

# School of Physics and Astronomy



## Gravitational wave searches associated with Galactic core-collapse supernovae

Scott Benjamin Coughlin

Submitted for the degree of Masters of Philosophy  
School of Physics and Astronomy  
Cardiff University

July 2015

# Summary of thesis

Understanding the mechanism by which stars become supernovae is a major unsolved problem in astrophysics. They are driven by the release of gravitational energy, which is expelled largely in the form of neutrinos. After almost 40 years of numerical simulations, it is still unclear how and why large stars explode. A core-collapse supernova (CCSN) begins when its core collapses and drives a shock wave outwards. Due to the emission of neutrinos and the inward pressure of the core collapse, the shock wave briefly subsides. The mechanism for the revival of the shock wave and subsequent supernova explosion is presently unknown. Proposed mechanisms include the neutrino, magnetorotational, and the acoustic mechanisms. Gravitational Waves (GWs) will help answer how large stars explode. The violent motions of dense matter in the stars core produce GWs, and their shape is determined by that motion. Therefore, the physical processes (i.e. either the neutrino, magnetorotational, or the acoustic mechanisms) can be inferred by studying the GWs. Estimates from numerical simulations indicate that the GWs from a supernova anywhere in the Milky Way would be strong enough to be detectable by advanced LIGO. A large burst of neutrino particles is also emitted in the core collapse; together with the GWs, these can determine the location of the supernova on the sky before the shock breakout, giving astronomers a chance to see the earliest stages of the explosion. Because the Galactic supernova rate is no larger than about one every thirty years, it is necessary for a search to be ready from the beginning of the operation of advanced LIGO. This search should include the ability to detect any plausible GW polarization that could arise from a CCSN. Specifically, the knowledge of the precise time and sky location of the SN provided by neutrino and optical detection respectively constrains how the GW signal will appear in a network of detectors. Thus, deviations from the expected detector response could reveal if GWs contain polarizations beyond those predicted by GR. This thesis explores the ability of aLIGO to detect scalar polarized GWs from CCSNe and other possible galactic sources.

# Declaration of authorship

- DECLARATION:

This work has not previously been accepted in substance for any degree and is not concurrently submitted in candidature for any degree.

Signed: ..... (candidate) Date: .....

- STATEMENT 1:

This thesis is being submitted in partial fulfillment of the requirements for the degree of Masters of Philosophy (MPhil).

Signed: ..... (candidate) Date: .....

- STATEMENT 2:

This thesis is the result of my own independent work/investigation, except where otherwise stated. Other sources are acknowledged by explicit references.

Signed: ..... (candidate) Date: .....

- STATEMENT 3

I hereby give consent for my thesis, if accepted, to be available for photocopying and for inter-library loan, and for the title and summary to be made available to outside organisations.

Signed: ..... (candidate) Date: .....

# Contents

<b>1</b>	<b>Introduction</b>	<b>1</b>
<b>2</b>	<b>Detection of scalar-polarized gravitational waves in the aLIGO era</b>	<b>5</b>
2.1	Gravitational Waves and core-collapse Supernova . . . . .	7
2.2	Overview of Scalar-Tensor Gravity . . . . .	8
2.3	Overview of Coherent Analysis . . . . .	10
2.3.1	Detection Statistic for Scalar Gravitational Waves . . . . .	12
2.3.2	Coherent Consistency Checks . . . . .	15
2.3.3	Benchmarking Performance . . . . .	16
2.4	Benchmarking the Scalar Search . . . . .	18
2.4.1	Choice of Scalar Waveforms . . . . .	19
2.4.2	Choice of Sky Location . . . . .	21
2.5	Galactic Search results . . . . .	22
2.5.1	Upper Limits . . . . .	22
2.6	Conclusion . . . . .	26
<b>3</b>	<b>Supernova Early Warning System Online Search</b>	<b>28</b>
3.1	Neutrino Detection of a Galactic Supernova . . . . .	28
3.2	Discussion of Supernova Waveforms . . . . .	30
3.3	SNEWS Triggered All-Sky vs. Optically Triggered Search . . . . .	32
3.4	SNEWS Benchmarking . . . . .	36
3.5	Conclusions . . . . .	39
<b>4</b>	<b>Conclusions</b>	<b>41</b>
<b>5</b>	<b>Appendix</b>	<b>43</b>
5.1	Appendix A: Likelihood Marginalization . . . . .	43
5.2	Appendix B: Detection Statistic Substitution . . . . .	44

# List of Figures

1.1	Cartoon illustrating GW polarizations. On the left is the deformation of space in the x and y-directions by a GW with a plus polarization. In red is the static case and blue is the case where the GW is at its maximum and minimum. In the middle is the deformation of space in the x and y-directions by a GW with a cross polarization. On the right is the deformation of space in the x and y-directions by a GW with a scalar polarization. . . . .	2
1.2	Illustration of the optical layout of a LIGO interferometer [1]. . . . .	3
2.1	Graphs demonstrating the effectiveness of coherent consistency checks. Top-Left: Null Coherent by Null Incoherent Energy. The square plot points represent the simulated GWB signals which appear on the left side of the E-I line and the crosses represent the background noise. As you can see the dashed red cut line recovers most of signals, while eliminating most of the background. Top-Right: Null Scalar Coherent versus Null Scalar Incoherent. Because the scalar signal is a single polarization the scalar coherent statistics have an additional scalar specific null stream. As with the null energy, the GWBs appear on the left side of the E-I line. Bottom: Scalar Coherent by Scalar Incoherent Energy. Again, as expected the simulated GWB signals appear on the right side of the E-I line. . . . .	17
2.2	A selection of the scalar waveforms used in this analysis. The $\alpha_0, \beta_0$ values are in parenthesis. Top-Left: Dust undergoing gravitational collapse to a BH ( $3.5 \times 10^{-3}, 0$ ) [2]. Top-Right: Model C CCSN explosion and subsequent formation of a NS, ( $4 \times 10^{-4}, -4$ ) [3]. Bottom-Left: sine-Gaussian waveform Bottom-Right: NS collapse to a BH, (0.025, -5) [4]. . . . .	20
2.3	Current constraints on the $\alpha_0, \beta_0$ parameter space. It is bounded by the Cassini probe experiments (under the black line) [5] and by the white dwarf J1738+0333 observations (under the blue line) [6]. The diamonds represent the original assumed values of $\alpha_0$ and $\beta_0$ for the various scalar waveforms considered and the squares are the new values used in the analysis done in this chapter. . . . .	22

2.4	These plots show the antenna response for the GR ( $F_+^2 + F_\times^2$ ) and scalar polarizations ( $F_b^2$ ) over the whole sky summed over different detector configurations H1L1 and H1L1V1 at a GPS time of 871728757. Top-Left: Shows the plus/cross response for H1L1V1 detector configuration. Top-Right: Shows the scalar response for H1L1V1 detector configuration. Bottom-Left: Shows the scalar response for H1L1 detector configuration. Bottom-Right: Shows the plus/cross response for H1L1 detector configuration. The overlaid 'x' marks the locations of the four sky points considered in this chapter. . . . .	23
2.5	Efficiency for a 1% false alarm rate threshold for a dust collapse and SN waveform injection using the scalar statistics formulated in this chapter. The four curves represent the four sky locations with the least sensitive recovery (farthest left) coming from the smallest antenna response to the scalar polarization and the most sensitive curve (farthest right) coming from the sky locations with the best scalar polarization response. Both models utilize $\alpha_0$ and $\beta_0$ parameters that are valid but on the fringe of the parameter space as indicated in 2.3: $(3.5 \times 10^{-3}, 0)$ and $(4 \times 10^{-4}, -4)$ . . . . .	24
2.6	Comparing detection efficiency of the scalar-mode search with that of the GR-mode search. For region of sky tested, see that scalar GWs are picked up by the GR search about as well as by dedicated scalar search. Yet, for the sky position with the best GR detector sensitivity compared with the scalar sensitivity (right plot) the distinction is even harder to make between the searches than the analysis where the opposite was the case (left plot). That is, the scalar sensitive was the best compared with the GR sensitivity. . . . .	25
2.7	Left: HL antenna response overlapped with a scatter plot of sky positions where the scalar and plus/cross polarization are distinguishable in value by more than 5 percent. Right: Same as left except with scalar antenna response. This figure highlights an unfortunate caveat when searching for a scalar signal with specialized statistics, the sky locations where the polarization are distinguishable are associated with extremely poor sensitivity to the scalar polarization. . . . .	26
2.8	Plot depicting "glitchiness" of the data. The Gaussianity measure is the $\frac{\text{variance}(S)}{\text{mean}(S)}$ in each frequency bin where S is the one-sided noise power. A value of 2 is expected for stationary Gaussian noise. The dotted lines indicate 3-sigma variations. Excursions to large values indicate the data is more variable than expected for Gaussian noise, i.e. "glitchy". Excursions to low values indicate low variability. The green and red dips to low values are due to large steady values of power that are associated with known events such as the 60Hz power lines. . . . .	27
3.1	A selection of the SN waveforms used in this analysis. Top-Left: Waveform from a 3D simulation of neutrino driven convection explosion mechanism from Ott [7]. Top-Right: Waveform from a 3D simulation of neutrino driven convection explosion mechanism from Mueller [8]. Bottom-Left: Waveform from a 2D simulation of a rotating CCSN from Dimmelmeier [9]. Bottom-Right: Waveform from a 3D simulation of a rotating CCSN from Scheidegger [10]. . . . .	32

- 3.2 This figure shows the summed antenna response to the plus and cross polarization of Hanford and Livingston ( $F_+^2 + F_\times^2$ ) overlaid with the linear search grid used in this search (dashed line). The solid line is the location of the Galactic Disk on the sky at this GPS time. The blue star at the intersection of the two lines represents the Galactic Center and is near the sky location used in benchmarking this search. 34
- 3.3 Left: The distribution of the significance (detection statistic), or “loudness”, of the background for the optical search using the logh-bayesiancirc statistic [11]. The black line represents the entire background before any coherent consistency cuts are made and the blue represents the surviving background. Right: Same as the left except for the linear grid search. There is no blue line in this case as no cuts were selected, so the blue and black lines are identical. . . . . 35
- 3.4 Left: Coherent versus Incoherent linear energy of the Ott 3D waveforms [7] in the optical search for the injection amplitude for which 90 percent of the injections were detected. The signals lie clear to the right of the E-I line and allow for an effective coherent cut selection. Right: Same as the left except for the linear grid search. This time a nontrivial number of the recovered signals energies lie on or on the opposite side of the E-I line. Although there are a number of injections whose statistics follow the expectation of the optical search, there are not enough in order to trigger a cut selection from the search. . . . . 35
- 3.5 The different coherent consistency cuts use different assumptions of polarization content. The GR cuts assume a plus and cross polarized signal, the circular cut assumes a circularly polarized signal, and the linear cut assume plus polarized signal only with an arbitrary polarizations angle. The -x refers to detection efficiency for the linear grid search which consists of a grid that is sufficiently dense over the sky without being too large to process quickly. The -o refers to the detection efficiency for an optically triggered, single sky point, search. Top-Left: A linearly polarized Dimmelmeier waveform [9]. Top-Right: A 3D Ott neutrino driven convection waveform [7]. Bottom-Left: A linearly polarized sine-Gaussian waveform. Bottom-Right: A 3D rotating core-collapse waveform from Scheidegger [10]. . . . . 37
- 3.6 Left: The distribution of the significance (detection statistic), or “loudness”, of the background for the optical search using the power-law statistic. The black line represents the entire background before any coherent consistency cuts are made and in both the linear grid and reduced linear grid no cuts were selected. Right: Same as the left except for the reduced linear grid search. Overall, the loudest background event is less significant in the reduced grid but by not a large margin. . . . . 38

3.7	Left: Coherent versus Incoherent linear energy of the Ott 3D waveforms [7] in the linear grid search for the injection amplitude for which 90 percent of the injections were detected. Again, the signals do not appear to have any consistent pattern. Right: Same as the left except for the reduced grid search. This time a more clear pattern is emerging as these signals are starting to clearly fall to the right of the E-I line. This improvement in the reduced grid suggests that, although the time delays are appropriately accounted for, the antenna response function may be miscalculated and the coherent combination of the data is incorrect for the linear grid search. . . . .	39
3.8	This figure shows the potential reduction in number of grid points of the linear grid search when utilizing information from the location of the MilkyWay on the sky. This information is over an arbitrarily chosen 48 hour period. The x-axis shows the percentage of the original number of grid points needed when the information from the MilkyWay is included. . . . .	39



# List of Tables

2.1	This table lists my parameter choices for the waveforms and sources in this analysis. The parameters that were modified from their original values are the distance, the $\alpha_0$ parameter and the mass. . . . .	21
2.2	This table lists the 50% detection efficiency distance at a false alarm rate of 1%. The values are derived from an equal weighted average across the four sky locations in our analysis. The detection distances for the waveforms with very large $\beta_0$ are due to the large amplitudes associated with models that assume $\beta_0 \neq 0$ . The asterisk indicates a waveform model whose $\beta_0$ value falls outside current constraints. . .	27
3.1	This table is taken from [12]. From left to right it provides the physical mechanism, literature reference, model name, the root sum square gravitational wave strain ( $h_{\text{rss}}$ ), the peak frequency of gravitational wave emission ( $f_{\text{peak}}$ ), the total energy emitted in gravitational waves ( $E_{\text{GW}}$ ) and polarizations for the numerical waveform injections utilized in this chapter. . . . .	31
3.2	We present the 50 percent detection distance at a false alarm probability of 0.1 percent utilizing the various coherent statistic and assumptions on polarization content. Across all waveforms, these coherent statistics provide nearly identical recovery distances. Nonetheless, the circular coherent consistency cuts proved best in 9 of the 10 waveforms.	40

I am grateful to many for this work. First of all, Penny Eagan, Jeana Evans and the Fulbright Scholarship through the United States Department of State provided me the wonderful opportunity to spend the year in Cardiff, and this would not be possible without their support for my entire time in the United Kingdom. In addition to Fulbright, I would like to thank the international scholarships team here at Cardiff University for their support. After hosting me for a summer program two years ago, Patrick Sutton was brave enough to take me on as a student and helped me immensely. Aside from Patrick, no person has helped me more this year than my brother Michael Coughlin. I could not have completed my thesis without him. Last but not least, I would like to thank the rest of my family for their support over this year, especially my Dad for encouraging me to take a chance and apply for the Fulbright, and my Mom for supporting me.



# Chapter 1

## Introduction

Einstein's general theory of relativity (GR) predicts that all accelerating objects with non-symmetric mass distributions produce gravitational waves (GW), which are oscillations in the space-time metric [13]. In the same way as light, gravitational effects do not propagate with infinite speed. Whenever the distribution of mass in a given system changes (for example, when one drops a basketball), the gravitational field adapts to this new mass distribution. The speed at which this change propagates is equal to the speed of light. The resulting change in the gravitational field is a GW.

GWs are predicted by any theory which assumes that gravitational effects propagate at finite speed. Characteristics such as the GW polarization, phase, and amplitude change depending on the theory assumed. It is for this reason that GWs can be used to test general relativity. In addition, they can be used to explore the physics of objects such as black holes, gamma-ray bursts, and supernovae above and beyond the information currently available from astronomy [13].

As GWs pass through space, space is contracted and expanded in directions orthogonal to the direction of propagation. According to GR, the GW can be decomposed into a linear combination of two transverse polarizations, known as plus and cross. Assuming the direction of propagation is along the z-axis, the plus polarization occurs in the x and y-directions and the cross along the two diagonals. Figure 1.1 shows these polarizations. The plus and cross components of GWs are exploited in order to detect them with interferometric detectors. There are alternative theories, however, which predict the existence of up to 6 polarizations [14, 15]. For the purposes of this thesis, I will explore the addition of one polarization transverse to direction of propagation, the breathing or scalar mode. Again, assuming the propagation is along the z-axis, the scalar polarization stretches the x-y space equally in all directions, also in figure 1.1. The scalar polarization arises from the addition of a scalar field to Einstein's field equations, as discussed in Section 2.2. Perturbations of this field cause scalar polarized GWs.

Before the observation of the binary pulsar system PSR 1913+16, GWs were strictly theoretical. Analysis of this system showed that the orbit of this neutron star pair lost energy at the rate predicted by General Relativity for GW emission[16]. Although there still exists no direct detection of GWs, this discovery provides indirect evidence for the existence of GWs. It, therefore, became useful to develop detectors in order to make direct findings. Over the past fifty years, a number of gravitational-wave detectors have been designed with various degrees of sophistication and purpose. Joseph Weber constructed and published results from the first

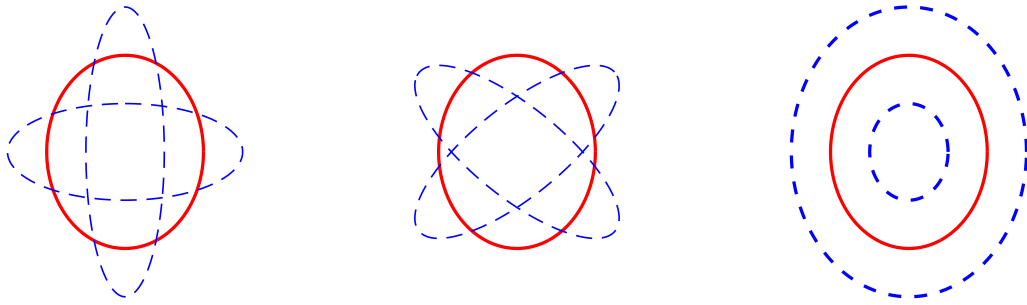


Figure 1.1: Cartoon illustrating GW polarizations. On the left is the deformation of space in the  $x$  and  $y$ -directions by a GW with a plus polarization. In red is the static case and blue is the case where the GW is at its maximum and minimum. In the middle is the deformation of space in the  $x$  and  $y$ -directions by a GW with a cross polarization. On the right is the deformation of space in the  $x$  and  $y$ -directions by a GW with a scalar polarization.

of these detectors. The analysis looked for strains caused by passing GWs in an aluminum bar [17]. Although he claimed a GW detection, it is likely these “detections” were only noise sources. Many, more sophisticated detectors exist today. Examples of this sophistication include that the detectors are seismically isolated and cryogenically cooled in order to reduce the natural vibrations in the bars and increase their sensitivity [18].

There exists a number of modern day interferometric ground-based detectors. The interferometric ground-based detectors are Michelson interferometers with Fabry-Perot cavities. This type of interferometer consists of a monochromatic light source, which today is almost exclusively a laser. Its light is sent to a beam splitter and sent down two orthogonal arms. At the end of each of these arms is a reflective mirror. The beams reflect off of these mirrors and recombine at the beam splitter, thereby sending a portion of the light toward a photodiode, and the remaining light back towards the laser. This photodiode outputs a current proportional to the average photon flux at the detector [19]. Any differential variation in the lengths of the arms will change the power seen at the photodetector. For example, if a GW passes through an interferometer perpendicular to its arms, space orthogonal to the direction of its motion will expand and contract. This will change the length of both arms, causing the power to modulate as function of time. Figure 1.2 shows a schematic for the LIGO interferometer.

Current ground-based detectors include LIGO [20], Virgo [21], and GEO600 [22]. LIGO consists of two 4 kilometer interferometers at Hanford, WA (H1) and Livingston, LA (L1) in the United States. Virgo consists of one 3 kilometer interferometer located in Pisa, Italy (V1). GEO consists of one 600 meter interferometer located in Hanover, Germany (G1). The LIGO detectors collected data as part of their fifth science run from November 4 2005 to September 30 2007 (S5) and Virgo collected data as part of its first science run from May 18, 2007 until September 30, 2007. The period starting May 18, 2007 is called the S5-VSR1 joint science run and is the period of data of interest for this thesis.

Future proposed underground detectors include the Einstein Telescope (ET) [23], and space-based detectors, such as LISA [24]. These experiments intend to provide direct detections of GWs and use that information to study certain astrophysical

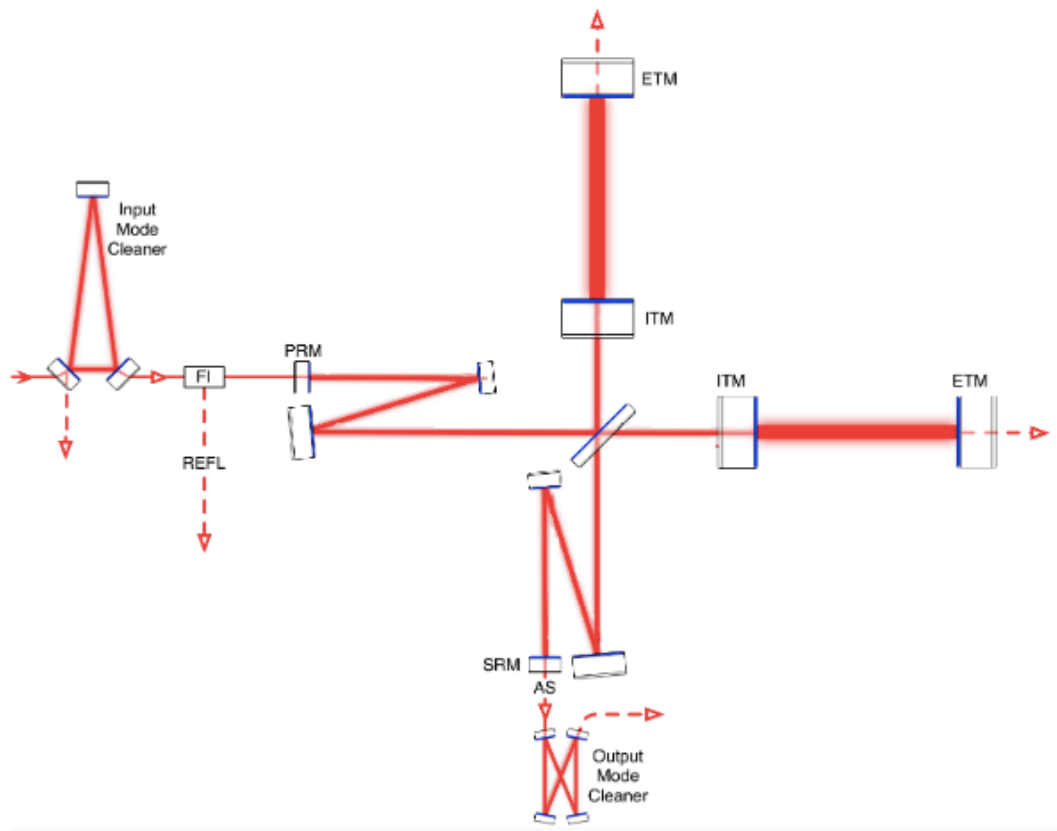


Figure 1.2: Illustration of the optical layout of a LIGO interferometer [1].

sources. Possible astrophysical sources that the detectors are sensitive to include the coalescence of massive binary systems containing massive objects such as neutron stars or black holes, the core collapse of a massive star into a Type II supernova, and processes from the time of the Big Bang that produce a stochastic background of GWs [25]. Because of their extremely small amplitudes, a direct detection of GWs from any of these systems is challenging. Their space displacements are on the order of  $10^{-18}$  m, which is a 1000 times smaller than the nucleus of an atom. In order to obtain sensitivity at these amplitudes, LIGO and Virgo use special interferometry techniques, state-of-the-art optics, highly stable lasers, and multiple layers of vibration isolation [20].

This thesis explores a variety of topics related to GW detection from Supernovae. It is organized as follows. In chapter 2, I discuss methods for the detection of scalar polarized GW signals. These include formulating signal processing statistics specific to the scalar mode and exploring the current viable scalar field parameter space. I also estimate the sensitivity of one of the LIGO standard data analysis packages, X-Pipeline, to these waveforms.

In chapter 3, I discuss the current implementation of the SuperNova Early Warning System (SNEWS) analysis. I describe how neutrino detection of a Galactic Supernova can guide a low-latency X-Pipeline analysis. I also assess sensitivity to SNe waveforms for two cases. First, the case where the precise location of the SN is known due to the optical observations. Second, the case before the optical SN is detected and only the neutrino early warning signal, with little or no sky location information, is available to guide the search. The latter analysis is performed in order to detect the GW signal before the optical detection in order to help direct the optical observers to the correct sky region to catch the earliest stages of the optical signal.

## Chapter 2

# Detection of scalar-polarized gravitational waves in the aLIGO era

Gravitational Wave Bursts (GWBs) have been sought as a source of gravitational waves from the beginning of gravitational-wave searches. Burst searches have ranged from GWBs associated with gamma-ray-bursts (GRBs) [11] to those associated with core collapse supernovae (CCSN) [26]. Previous burst searches focused on detecting the polarizations predicted by GR, plus and cross [27], as well as special cases of the plus and cross polarization, the circular [11] and linear [26] polarization. In this paper, I will refer to searches that assume any of these polarizations as a standard GWB analysis.

Typical gravitational-wave searches for GWBs employ the technique of a coherent analysis [27–31]. A coherent analysis uses both individual and combined detector data streams in order to better reject background noise events and thereby increase sensitivity to GWBs. The idea behind using combined and individual data streams is that GWBs will appear in some quantifiable capacity in all the data streams, but loud data transients, called “glitches,” would typically occur in only one of the detectors at a given time.

In our analysis, I use and modify a software package known as “X-Pipeline” [27]. X-Pipeline has been used as a search algorithm for GWB sources such as GRBs and CCSN in initial LIGO searches. For these astrophysical events, the algorithm uses sky location information of the source to tune the analysis. In the standard analysis, the detectors will have different sensitivities to a plus and cross polarized GWB from different sky directions. These responses can be mathematically modeled and various likelihood statistics calculated to extract time-frequency pixels from the data that are more likely to be GWBs [32]. In this work, I use these same standard statistics but modify them for the scalar mode and compare the performance of scalar versus standard statistics when searching for scalar GWBs.

Most previous work in GWBs used the GR framework for their searches. In general, this was reasonable because energy in the form of gravitational radiation is expected to be stronger in the standard modes than the alternative modes. The weaker energy can be traced to the  $\omega$  coupling parameter in the Brans-Dicke-Jordan-Fierz theory. This parameter is a value that ensures scalar-tensor theories are consistent with current observations. That is, GR has passed all tests to this point. Therefore, any deviations from GR must be relatively small which is exemplified by the  $\frac{1}{\omega}$



parameter. The limit of Brans-Dicke as  $\omega$  approaches infinity is standard GR [14]. The solar system experiment carried out by the Cassini probe placed a constraint on  $\omega$  of greater than  $4 \times 10^5$  [5], although recent papers [33, 34] suggest even stronger constraints can be placed on this value through the detection of gravitational-waves. Despite this small value of  $\frac{1}{\omega}$ , scalar gravitational waves are worth considering with respect to a SNe. This is because spherically symmetric systems cannot produce GWs in GR, but they can emit scalar polarized signals. Therefore, in nearly symmetric systems such as SNe, they could be the dominant form of the GWs produced. This chapter also explores other nearly spherically symmetric systems such as a Neutron Star (NS) collapse to a Black Hole (BH) and the spontaneous scalarization of a NS.

The advanced detector era, which includes advanced LIGO [1], advanced Virgo [35], KAGRA [36] and begins operations in late 2015, provides new hope for detecting standard and alternative gravitational-wave polarizations. In particular, the proposed search for GWBs associated with a Galactic Supernova (GS) is especially promising. The nearby distance of the source and increased sensitivity of the advanced era detectors make the search for alternative gravitational wave modes a tempting proposition. Also, these factors could mean that the current sky-localized burst searches, as they are currently implemented, could potentially detect scalar GWBs. GWs from the next GS will provide a wealth of information concerning SNs. This includes learning information such as the structure of massive stars, core collapse dynamics, and the still uncertain CCSN explosion mechanism [37]. In addition, GWs could provide insight into explosive nucleosynthesis and mixing of synthesized elements that occur during the explosion as well as insight into fundamental physics such as the equation of state of nuclear matter and neutrino interactions [38].

In this chapter, I benchmark the feasibility of searching for scalar polarized waveforms from a source such as a galactic CCSN, and determine the sensitivity of the standard sky-localized burst search with respect to the scalar polarization in the early aLIGO era. I emphasize the sky-localized aspect of the search because previous work has explored this question in relation to all-sky burst searches [39]. Initial work demonstrated that these searches are sensitive to these waveforms, but the recovered sky location in many cases was demonstrated to be poor. This effect occurs because the all-sky search incurs a degeneracy of the scalar signal with the GR signal. That is, a scalar signal from direction  $\Omega_1$  may look similar in the network to a GR signal coming from direction  $\Omega_2$ . A triggered search removes this degeneracy because  $\Omega$  is known beforehand. In principle, this makes it possible to distinguish the scalar signal from the GR signal, motivating a more extensive study for burst searches that utilize sky position as part of the search.

For the advanced detector era there are three major benefits of such an analysis. First, it provides evidence for the feasibility, or lack thereof, that burst searches utilizing sky localization of the source in their search would capture a scalar polarized waveform. As all present burst searches assume standard polarizations, it will suggest whether follow-up runs for different theorized polarizations for these searches should be conducted at some point. If the efficiency of detection is only marginally less in the specially designed search, then it would inform the priorities of performing this type of search. Second, it provides evidence at what distances a scalar polarized waveform could feasibly be detected by the detectors. If the scalar waveforms prove too quiet to be detectable, then follow-up searches for some events would be unnecessary. This is vital to the Supernova Neutrino Early Warning Sys-

tem (SNEWS) triggered search planned for the early aLIGO science runs [40]. I also address whether or not an implementation of the scalar search should be included as part of a follow-up to such an alert.

In section 2.1, I discuss why GW emission mechanisms from CCSNe provide good sources for GWs. In section 2.2, I provide a summary of the scalar polarization and perform a brief literature review of the GW applications. In section 2.3, I give an overview of the X-Pipeline algorithm and its modifications that I made for the scalar search. In section 2.4, I discuss the factors that went into selecting the waveforms and supernovae used to benchmark the GR and scalar searches. In section 2.5, I present our results from the simulated SNEWS-like search using the scalar analysis. In section 2.6, I offer concluding remarks and suggest directions for future research.

## 2.1 Gravitational Waves and core-collapse Supernova

In this section, I briefly explain the process of a core-collapse supernova, including how they emit GWs, why a detection is anticipated, and what potential information is associated with those GWs (please see [37] and references therein for further information).

When a massive star on the order of  $> 10M_{\odot}$  explodes, the stellar core collapses to a hot proto-neutron star. After, the proto-neutron star cools down through neutrino emission. Next, the collapse halts suddenly when the collapsing iron core reaches neutron-star density. The collapse over-shoots equilibrium density, causing a rebound, the “bounce”, that launches a shockwave. When the shockwave reaches the surface of the star, it lights up the star in a supernova explosion. The mystery in this process is that the shockwave is not energetic enough to plow through the stellar mantle. In theory, the absorption of a small fraction ( 10%) of the neutrinos within the first second after the creation of the proto-neutron star fuels the shockwave. In particular, the neutrinos heat up the collapsing mass above the proto-neutron star which drives convection. This convection provides one source of GWs from CCSNe. The heated material at the bottom of the stellar material will rapidly rise in comparison to the cool stellar mass towards the mantle of the star. This bulk motion of large quantities of material leads to the emission of GWs. Other sources of GWs from the CCSN depend on other variables. If, for instance, the star’s core is spinning prior to core collapse, then the initial creation of the proto-neutron star will emit a burst of GWs lasting only a few milliseconds. In Sections 3.2 and 2.4.1, I discuss CCSN waveforms in more detail.

Depending on the distance of the CCSN, Earth based detectors can detect the neutrinos from this process. For example, Super Kamiokande (Super K), one of these Earth-based neutrino detectors, detected neutrinos from the last GS, supernova SN 1987A, which exploded in the Large Magellanic Cloud. Unfortunately, in 1987 no detectors sensitive enough to CCSN GWs existed. As discussed in the introduction, the planned sensitivity of the next generation of GW detectors along with theoretical predictions of the GW emission from CCSNs [37] suggest there is a chance of detecting GWs from a CCSN in the Milky Way. In addition to the close distance of a CCSN in the Milky Way, the other cause for optimism is because the neutrinos from the supernova will be detected by detectors such as Super K [41]. These detectors will provide a precise timestamp of the event which will help guide the GW search.

The observation and characterization of GWs from the next GS will provide

information unattainable through optical analysis. First, in the CCSN context, GWs directly probe the uncertain degree of asymmetry of the supernova engine because they are produced by bulk aspherical accelerated motion of mass-energy. For instance, the angular momentum of the collapsing core can be measured using GWs from rotating core collapse, see [42, 43]. Second, GWs are expected to be emitted by a broad range of processes, e.g. [37, 38], many of which can be directly associated with particular explosion mechanisms. This means that GWs can either eliminate or validate various theoretical explosion mechanisms. For example, the neutrino explosion mechanism links to the GW signal from the neutrino-driven convection and the magnetorotational explosion mechanism links to a strong signal from a rotating CCSN, see [44, 45]. Moreover, the moment of the onset of explosion can be inferred and the structure of the nascent neutron star can be constrained through the detection of GWs from neutrino-driven convection and the standing accretion shock instability. With this information, constraints can be placed on the nuclear equation of state [8, 46, 47]. Finally, the abrupt end of GW and the simultaneous neutrino emission would indicate the formation of a black hole, see [48, 49]. As such, a GW detection will clarify much of the unknown physics that occurs as a star transitions from collapse to explosion.

This potential wealth of science has motivated work towards understanding GW emission from CCSN and quantifying with varying degrees of refinement the detectability of the GWs. Examples of this work include theoretical estimates of optimal or angle-averaged signal to noise ratios, see [37], sensitivity estimates based on real data that has been rescaled to match the expected noise characteristics of aLIGO in its first observing run, [12] and an ongoing search to detect or place upper limits on GWs from an extra-galactic CCSNe in initial LIGO data [26]. These studies show that a galactic CCSN at a distance of a few kpc may be detectable by the advanced LIGO detectors in their first observing run in late 2015, referred to as the O1 observing run. With a detection, focus will shift towards waveform reconstruction and parameter estimation in order to determine some of the important astrophysical questions poised above. CCSN occurring at distances beyond the Milky Way are unlikely to be detectable with the projected advanced detectors sensitivity on the basis of current GW signal predictions from detailed multi-dimensional simulations, see [7, 8, 37]. However, useful science can be sought and obtained from more distant CCSN in the case of extreme emission scenarios associated with longer-lasting (few seconds) bar-mode instabilities, see [50] or fragmenting accretion disks, see [51].

These estimates and studies have, however, only been conducted on models and simulations assuming plus and cross polarized signals. No work has yet been conducted on detecting scalar polarized signals. The detection of scalar GWs would provide both insights into the CCSN physics and revolutionize our understanding of gravity and space-time. These factors motivate the importance of determining the feasibility of detecting scalar GWs.

## 2.2 Overview of Scalar-Tensor Gravity

In this section, I discuss the basic idea of scalar gravitational waves. For a thorough analysis of the addition of the scalar field to standard GR, see [52]. I discuss only aspects of the theory that are important to this analysis.

Figure 1.1 shows the three polarizations of GWs of interest for this analysis, the

cross, plus and breathing mode. Essentially, a scalar field is added to the standard Einstein field equations and perturbations of this 0-spin field  $\phi$  create scalar polarized GWs. With the addition of this 0-spin field, the action now has the form

$$I = (16\pi)^{-1} \int \sqrt{-g} \left( \phi R - g_{\mu\nu} \frac{\omega(\phi)}{\phi} \delta_\mu \phi \delta_\nu \phi \right) d^4x + I_m[\Psi_m, g_{\mu\nu}] \quad (2.1)$$

where  $\omega(\phi)$  is an arbitrary function and  $I_m$  is the action for the matter fields  $\Psi_m$ . Equation 2.1 is in the so-called Brans-Dicke frame. In order to get from the Brans-Dicke frame into the more commonly used Einstein frame, two terms need to be defined

$$\frac{1}{G_* A^2(\varphi)} = \phi \quad (2.2)$$

and

$$\alpha^2(\varphi) = \frac{1}{3 + 2\omega(\phi)}. \quad (2.3)$$

In Brans-Dicke theory,  $G_*$  is the value of Newton's constant in asymptotic limit and  $\phi$  is a constant. In this way,  $\alpha(\varphi)$  and, by design, the  $\omega(\phi)$  are constant.  $A(\varphi)$  and  $\alpha(\varphi)$  relate in the following way

$$\alpha(\varphi) = \frac{d \ln A(\varphi)}{d\varphi}. \quad (2.4)$$

With these substitutions, the action now has the form

$$I = (16\pi G_*)^{-1} \int d^4x \sqrt{-g_*} (R_* - 2g_*^{\mu\nu} \delta_\mu \varphi \delta_\nu \varphi) + I_m[\Psi_m, A^2(\varphi) g_{\mu\nu}^*] \quad (2.5)$$

where  $g_{\mu\nu} = A^2(\varphi) g_{\mu\nu}^*$ . It is clear that as  $\alpha(\varphi) \rightarrow 0$  or equivalently  $\omega(\phi) \rightarrow \infty$  then  $A^2(\varphi)$  will approach 1 and the equations revert back to the standard Einstein equations.

In most studies, the function  $\alpha(\varphi)$  is assumed to take the form of a Taylor expansion

$$\alpha(\varphi) = \alpha_0 + \beta_0(\phi - \phi_0) + \beta_1(\phi - \phi_0)^2 + \dots \quad (2.6)$$

For all models in this chapter,  $\alpha(\varphi)$  is defined by the two variable parameter space of  $\alpha_0$  and  $\beta_0$ :

$$\alpha(\varphi) = \alpha_0 + \beta_0(\phi - \phi_0). \quad (2.7)$$

Finally, I can now define  $A(\phi)$  in terms of  $\alpha_0$  and  $\beta_0$ .

$$A(\varphi) = e^{\alpha_0(\phi - \phi_0) + \frac{1}{2}\beta_0(\phi - \phi_0)^2} \quad (2.8)$$

One potentially exciting result of the addition of a scalar field to standard theory is that a perturbed scalar field will emit monopole and dipole GWs instead of just quadrupolar GWs. Dipolar waveforms would be expected in binary coalescences. For a review of alternative theories of gravity and how their inclusion impacts data analysis in the case of compact binary coalescences of neutron stars and black holes, please see [15]. I concentrated on the scalar polarization which would result from

spherically symmetric systems of which core-collapse supernovae provides a potential source. Research has been conducted to benchmark current all-sky burst search algorithms, such as coherent Wave Burst (cWB) [39], to scalar waveforms. Preliminary results found the all-sky search to be sensitive to the scalar polarization with the standard (GR) search, but these results showed that recovered versus injected sky-location was very different. Because of this, I decided to explore the impact of sky localized searches on scalar GWs. It is also important to separate this analysis from research that is on-going in constraining alternative gravity with the detection of GWs. Without more than three detectors, it is impossible to determine whether a detected GW event was, in fact, scalar polarized, due to the degeneracy with the longitudinal mode [53]. To decouple the two, at least four detectors would be required. Determining whether a GW possessed an alternative polarized signal is not the purpose of this study. I simply aim to assess the detectability of a scalar polarized signal by itself. The determination of the exact polarization of the signal is left to a future study.

## 2.3 Overview of Coherent Analysis

An overview of the standard method and notation of an X-Pipeline analysis now follows (for a more complete discussion, see [27]). A GWB search has three necessary components, the sky location  $\Omega$ , the detector data  $d$  for a given detector  $\alpha$  and the characterization of the GW in the plus and cross polarizations,  $(h_+(t), h_\times(t))$ . The detector data  $d$  can be further subdivided into two component parts. These parts are the data that is background noise  $n$  and the data that is signal, which is given by the detector response  $F_\alpha(\Omega)^+$  and  $F_\alpha(\Omega)^\times$ , multiplied by the signal. The sky location plays two roles in this analysis. First, given a sky location, I know the exact time-of-arrival delay, written as  $\Delta t_\alpha(\Omega)$ , of the GW signal between the various detectors. Second, I can use the sky location to calculate the detector responses to the signal. These functions have the form

$$\mathbf{F}^+(\Omega) = \frac{1}{2}(1 + \cos^2 \theta) \cos 2\phi \cos 2\psi - \cos \theta \sin 2\phi \sin 2\psi \quad (2.9)$$

$$\mathbf{F}^\times(\Omega) = -\frac{1}{2}(1 + \cos^2 \theta) \cos 2\phi \cos 2\psi - \cos \theta \sin 2\phi \sin 2\psi. \quad (2.10)$$

Here,  $\phi$  is the azimuthal angle of the source in detector-based coordinates,  $\theta$  is the polar angle of the source in Earth-Centered coordinates, and  $\psi$  is the polarization angle of the GW. Because Equation (2.9) and (2.10) are written in detector-based coordinates both  $\theta$  and  $\phi$  vary with time.

With this in mind, I characterize the data as a function of time as follows,

$$d(t + \Delta t_\alpha(\Omega)) = F_\alpha(\Omega)^+ h_+(t) + F_\alpha(\Omega)^\times h_\times(t) + n_\alpha(t + \Delta t_\alpha(\Omega)). \quad (2.11)$$

Now, if I apply a time shift of the individual detector streams corresponding to  $\Delta t_\alpha(\Omega)$ , then I obtain the simultaneous contributions of energies among the detectors that would contain the GWB. After this time-shift is performed, only a time- series

of detector strains remains. At this point, searches for GWBs move from the time-domain to the frequency-domain in the form of time-frequency maps proportional to GW strain power. The pixels of these time-frequency maps are computed by dividing detector strain time series in segments and computing Fourier transforms of the segments. The Fourier transform of the strain data from detector  $\alpha$  for the segment with a mid-time of  $t$  is denoted  $\tilde{s}_\alpha(t; f)$ . For the results presented here, I use 50%-overlapping, Hann-windowed segments with fast-fourier transform (FFT) lengths ranging from  $\frac{1}{2}$  s to  $\frac{1}{128}$  s. I utilize a range of TF-pixel sizes because I do not know ahead of time what pixel size will best capture the GWB. The one-sided noise spectrum for detector  $\alpha$  is defined as  $S_\alpha(f) = ((\tilde{s}_\alpha(t; f))^2)/T$ , where  $T$  is the FFT length. During this process I also whiten the data, which accomplishes the results of a relatively flat Fourier spectrum of our time series of data. Thus, for a given pixel of center time  $t$  and frequency  $f$ , a new equation can be written that characterizes the data as,

$$\mathbf{d} = \mathbf{F}^+ h_+ + \mathbf{F}^\times h_\times + \mathbf{n}. \quad (2.12)$$

where the boldface variables are vectors with  $D$  dimensions, i.e. the number of detectors. Specifically, each variable expands as follows:

$$\mathbf{d} = \begin{bmatrix} d_1(t, f)/\sqrt{S_1(f)} \\ \vdots \\ d_D(t, f)/\sqrt{S_D(f)} \end{bmatrix} \quad (2.13)$$

$$\mathbf{n} = \begin{bmatrix} n_1(t, f)/\sqrt{S_1(f)} \\ \vdots \\ n_D(t, f)/\sqrt{S_D(f)} \end{bmatrix} \quad (2.13)$$

$$\mathbf{F}^{+, \times} = \begin{bmatrix} F_1^{+, \times}(t, f)/\sqrt{S_1(f)} \\ \vdots \\ F_D^{+, \times}(t, f)/\sqrt{S_D(f)} \end{bmatrix} \quad (2.13)$$

The noise and detector response are each normalized by the square root of the one sided noise power spectrum  $S_i(f)$  of the detectors.

In their present states, the detector data streams that have been whitened and FFTed have not been transformed to maximize the benefit of analytically writing the data as I have in Equation (2.12). To do so, I make a change of orthonormal basis. In its present form, the superfluous detector noise  $\mathbf{n}$  is uncorrelated between the detectors and thus its covariance matrix would be unchanged through a change in basis. Given the form of Equation (2.12) the natural choice for the new basis of the detector data streams is  $\mathbf{F}^+$  and  $\mathbf{F}^\times$ . This basis of the detector data will work for two or more detectors, where the first two streams span the  $\mathbf{F}^+$  and  $\mathbf{F}^\times$  and the remaining  $D-2$  streams are null streams which are orthogonal to the  $\mathbf{F}^+$  and  $\mathbf{F}^\times$  plane. Once transformed to this new basis, the streams no longer correspond to any single detector. The final transformation performed on our data characterization is to further transform the  $\mathbf{F}^+$  and  $\mathbf{F}^\times$  basis by selecting the polarization basis such that  $\mathbf{F}^+$  and  $\mathbf{F}^\times$  are orthogonal and  $\|\mathbf{F}^+\| \geq \|\mathbf{F}^\times\|$ . In this special basis,  $\mathbf{F}^+$  and  $\mathbf{F}^\times$  are denoted by  $\mathbf{f}^+$  and  $\mathbf{f}^\times$ . This basis is called the Dominant Polarization

Frame [28]. It is here that I make a key remark. The value  $\mathbf{e}^+ = \frac{\mathbf{f}^+}{\|\mathbf{f}^+\|}$  and  $\mathbf{e}^\times = \frac{\mathbf{f}^\times}{\|\mathbf{f}^\times\|}$  represent our template for what a GWB signal looks like in the data. Essentially, it is template based on signal amplitude. The benefit of characterizing and transforming the data in this manner is twofold. First, there are two unknown values in each pixel,  $(h_+(t), h_\times(t))$ , and with three or more data samples, i.e. detectors, per pixel then it is possible to solve for these quantities. It would be possible to solve with only two data samples if there was no noise. With only two detectors and the addition of a time constraint on the coincidence of candidate events, which are “loud” groups of TF-map pixels clustered together, however, then I can determine  $(h_+(t), h_\times(t))$ . Second, and in a similar line of reasoning, this basis can be used to construct two types of statistics: detection or ranking statistics and coherent consistency statistics. A detection statistic is used to determine the probability that a given data segment contains a gravitational-wave signal and will be discussed in Section 2.3.1. Coherent consistency tests, on the other hand, are used to reject spurious noise transients which can be confused as a signal by these ranking statistics if not eliminated beforehand and will be discussed in Section 2.3.2.

### 2.3.1 Detection Statistic for Scalar Gravitational Waves

This analysis relies on incorporating the above coherent analysis for GR polarizations, to an identical analysis for the scalar polarization. For a robust multi-polarized GW signal search, this would entail characterizing the data as

$$\mathbf{d} = \mathbf{F}^+ h_+ + \mathbf{F}^\times h_\times + \mathbf{F}^b h_b + \mathbf{n}, \quad (2.14)$$

and then finding an orthonormal basis and utilizing four or more detectors to extract the signal. I propose a different analysis, however, as the multi-polarized search has two major challenges. First, in the early advanced detector era, only Hanford and Livingston are expected to be running in coincidence. Also, a fourth detector is not expected for another decade. Second, our source object is a CCSN which, if it undergoes near perfect spherically symmetric collapse and there are alternative polarization to those predicted by GR, it is possible that most of that energy will be in the form of monopole radiation. Therefore, I propose a simplified analysis where the data is characterized as exclusively a scalar GW and modify existing GR detection and coherent statistics for that polarization. The data model simplifies to

$$\mathbf{d} = \mathbf{F}^b h_b + \mathbf{n}. \quad (2.15)$$

In the case of the scalar polarization, it is unnecessary to transform the antenna response function into the dominant polarization frame because there is only the one mode. More precisely, this signal is already linearly polarized and so the basis  $\mathbf{F}^b$  is already maximized to the scalar signal. The scalar mode antenna response function has the form [15]

$$\mathbf{F}^b(\theta, \phi) = \frac{1}{2} \sin^2 \theta \cos 2\phi. \quad (2.16)$$

For consistency with the GR case, however, I refer to “dominant polarization” antenna response as  $\mathbf{f}^b$ . Also, as before, I define our template for a scalar GWB as the unit vector in the scalar frame: the scalar antenna response over the norm of the response,  $\mathbf{e}^b = \mathbf{f}^b / \|\mathbf{f}^b\|$ .

Our formulation of the breathing mode coherent and detection statistics is as follows. For a complete treatment of this issue, see [32]. First, I start with the familiar matched-filter likelihood ratio [54]

$$L = \frac{p(\mathbf{d}|h_b, \mathbf{n})}{p(\mathbf{d}|\mathbf{n})}. \quad (2.17)$$

For this ranking statistic, the assumption is the noise is Gaussian. This allows the denominator of our equation to be written as.

$$p(\mathbf{d}|\mathbf{n}) \propto \exp\left(-\frac{1}{2} \int_{-\infty}^{\infty} \frac{2|\mathbf{d}|^2}{S_f} df\right). \quad (2.18)$$

The numerator takes the form

$$p(\mathbf{d}|h_b, \mathbf{n}) \propto \exp\left(-\frac{1}{2} \int_{-\infty}^{\infty} \frac{|(\mathbf{d} - h_b)|^2}{S_f} df\right). \quad (2.19)$$

Now rewrite Eq. 2.17 as,

$$L = \frac{p(\mathbf{d}|h_b, \mathbf{n})}{p(\mathbf{d}|\mathbf{n})} = \frac{\exp\left(-\frac{1}{2} \int_{-\infty}^{\infty} \frac{|(\mathbf{d} - h_b)|^2}{S_f} df\right)}{\exp\left(-\frac{1}{2} \int_{-\infty}^{\infty} \frac{2|\mathbf{d}|^2}{S_f} df\right)}. \quad (2.20)$$

By taking the log, the above equation reduces to

$$2 \log(L) = -||(\mathbf{d} - h_b)||^2 + ||\mathbf{d}||^2 = 2(\mathbf{d} \cdot h_b) - ||h_b||^2 \quad (2.21)$$

where  $||a||^2 = a \cdot a$  and

$$a \cdot b = \int_{-\infty}^{\infty} \frac{a^*(f)b(f)}{S(f)} df \quad (2.22)$$

where  $*$  is the complex conjugate.

I now can define the signal to noise ratio (SNR). The SNR is the expected value of the log-likelihood ratio over all noise realizations. The SNR is as follows

$$\begin{aligned} E[2 \log(L)|\mathbf{d} = h_b + n] &= E[\mathbf{d} \cdot h_b + \mathbf{d} \cdot n - \cdot h_b^2] \\ &= 2||h_b||^2 - ||h_b||^2 = ||h_b||^2. \end{aligned} \quad (2.23)$$

The above analysis was performed by assuming that the signal was known perfectly beforehand. That is, that the template signal and the real signal were the same. In reality, I know this is not the case and that the signal in the data will be different from our template. In the case of burst searches this is because our template is a time-frequency pixel with energy,  $\mathbf{e}^b$ . So, let  $h_b^*$  represent the signal as found in the data and then the SNR becomes the

$$E[2 \log(L)|\mathbf{d} = h_b^*] = \max_{h_b} (2(h_b^* \cdot h_b) - ||h_b||^2). \quad (2.24)$$

Now, I must determine the factor of our template  $h_b$  that I believe to be the unknown component. The most significant unknown factor in the determination of signal  $h_b$  is its amplitude. Therefore, I write  $h_b$  as  $A \frac{h_b}{||h_b||}$ . Maximizing over amplitude A,

$$\max_{A, h_b} \left( 2 \left( h_b^* \cdot A \frac{h_b}{||h_b||} \right) - ||A \frac{h_b}{||h_b||}||^2 \right). \quad (2.25)$$



After taking the first derivative with respect to  $A$  and setting it equal to zero, I arrive at  $A = \frac{h_b^* \cdot h_b}{\|h_b\|^2}$ . Finally, after incorporating this characterization of the amplitude, the appropriate matched-filter detection statistic is as follows

$$S_{MF} = \max_{h_b} \left( \frac{(h_b^* \cdot h_b)^2}{\|h_b\|^2} \right). \quad (2.26)$$

I now explore the Bayesian framework for creating the scalar detection statistic. The intuitive difference between these two frameworks is as follows. Bayesian inference is designed in order to just determine whether the data contains a signal or not. The match filter statistic, however, relies on the concept of templates as a way to produce a likelihood of a signal existing in the data or not. Put more simply, I aim to limit the assumptions I make when creating a detection statistic, and because the template signal is not very reliable in the case of a GWB, it is advantageous to use the Bayesian framework which does not rely on templates. The marginalized likelihood takes the form

$$L(\mathbf{d}) = \int_{h_b} L(\mathbf{d}|h_b)p(h_b)dh_b. \quad (2.27)$$

The two components I must determine for this analysis are an appropriate prior  $p(h_b)$  and the form of  $L(\mathbf{d}|h_b)$ . In calculating the former, I must separate the signal  $h_b$  into its unknown components. Like the matched-filter analysis, the most significant unknown is the amplitude. Therefore, for this statistic, I assume that the strain of the actual waveform has a Gaussian distribution of width  $\sigma_h$ . More precisely, I assume that a characteristic burst signal will have some strain  $\sigma_h$  in the range  $[10^{-23}, 10^{-21}] \text{Hz}^{-\frac{1}{2}}$  [55]. As before, I separate out the part of the template that is the amplitude and call it  $A$ . Therefore, I rewrite  $h_b$  as  $A \frac{h_b}{\|h_b\|}$  and the  $p(A)$  is

$$p(A) = \frac{1}{\sqrt{2\pi\sigma_h^2}} \exp\left(-\frac{1}{2} \frac{A^2}{\sigma_h^2}\right). \quad (2.28)$$

This choice of  $\sigma_h$  allows us to integrate out the amplitude, but I must rewrite  $L(\mathbf{d}|h_b)$  as  $L(\mathbf{d}|Ah_b, \sigma_h)$ .

$$L(\mathbf{d}) = \int_{h_b, \sigma_h, A} L(\mathbf{d}|Ah_b, \sigma_h)p(A)p(\sigma_h)p(h_b)dAd\sigma_h dh_b. \quad (2.29)$$

For a complete treatment of integrating out the amplitude please see Appendix 5.1. When the marginalization is complete, I am left with a log-likelihood value of

$$\log(L(\mathbf{d}|h_b, \sigma_h)) = \frac{(\mathbf{d} \cdot h_b)^2}{\|h_b\|^2 + \frac{1}{\sigma_h^2}} - \log(\sigma_h \|h_b\|^2 + 1) \quad (2.30)$$

The above analysis may look familiar, but a key substitution is necessary in order to incorporate it into our present analysis framework. In our framework, the value of the normalization of the template signal  $h_b/\|h_b\|$  is actually  $\mathbf{e}^b = \mathbf{f}^b/\|\mathbf{f}^b\|$ . This changes the matched-filter and Bayesian inference formulation to

$$\log(L(\mathbf{d}|h_b, \sigma_h)) = \frac{(\mathbf{d} \cdot \mathbf{e}^b)^2}{1 + \frac{1}{(\sigma_h \|\mathbf{f}^b\|)^2}} - \log(\sigma_h \|\mathbf{f}^b\|^2 + 1) \quad (2.31)$$

$$S_{MF} = \max_{h_b} \left( \frac{(h_b^* \cdot h_b)^2}{\|h_b\|^2} \right) = \max_{\mathbf{e}^b} (h_b^* \cdot \mathbf{e}^b)^2 \quad (2.32)$$

See Appendix 5.2 for a complete treatment of this substitution. The important similarity between these two statistics is that the numerator  $(h_b^* \cdot \mathbf{e}^b)^2$  is applied to some threshold. In fact, following [32] it can be shown that both of these statistics reduce to the same quantity when the waveform template is very well known beforehand. However, in burst searches, this is not the case and it is therefore useful to use Bayesian inference.

I am still not finished with the Bayesian inference approach, however, as it is still necessary to marginalize out the characteristic burst strain  $\sigma_h$ . I marginalize over a discrete set of strains,  $\Sigma$ . As mentioned previously, I select signals covering  $[10^{-23}, 10^{-21}] \text{Hz}^{-\frac{1}{2}}$ . I assume a prior of  $\frac{1}{\sigma_h}$  which corresponds to log-spaced values of  $\sigma_h$ . From this, the final statistic looks as follows

$$L(\mathbf{d}) = \log \left( \sum_{\sigma_h \in \Sigma} \frac{1}{\sigma_h} \exp(L(\mathbf{d}|h_b, \sigma_h)) \right) \quad (2.33)$$

### 2.3.2 Coherent Consistency Checks

One critical assumption prevalent throughout the discussion of the detection or ranking statistic section was the idea that the background noise distribution was consistent with Gaussian noise. However, in reality I know that the noise is filled with loud noise transients, also known as glitches. The attempt to make the background noise Gaussian motivates the next section and highlights a significant advantage of the coherent analysis. In general, loud noise transients are uncorrelated among the detectors, unlike the gravitational wave signal, and therefore I can compute statistics and perform tests to eliminate these transients. In the analysis, I take the data  $\mathbf{d}$  and project it onto the null space, i.e. the space orthogonal to the unit orthonormal basis  $\mathbf{e}^b$ , defined as  $\mathbf{e}^n$ . In this framework, I can now define two terms, the coherent and incoherent null energy labelled as  $E_n$  and  $I_n$ , respectively. For  $\alpha, \beta \in D$  where  $D$  is the number of detectors, the projection operator takes the form

$$E_n = \|\mathbf{e}^n \cdot \mathbf{d}\|^2 = \sum_{\alpha, \beta} e_\alpha^{n*} e_\beta^n d_\alpha^* d_\beta \quad (2.34)$$

$$I_n = \sum_{\alpha} e_\alpha^{n*} e_\alpha^n d_\alpha^* d_\alpha = \sum_{\alpha} \|e_\alpha^n\|^2 \|d_\alpha\|^2 \quad (2.35)$$

where  $*$  represents the complex conjugate of the variable. The important determination with these statistics is to calculate where a GWB would be expected to fall on a line of equal coherent and incoherent energy, which I will call the  $E - I$  line. To understand this, I can think of this statistic in terms of the discussion concerning detection statistics. Instead of taking the match-filter statistics of Equation (2.17), I took the maximum likelihood ratio of

$$L = \frac{\max_{h_b} (p(\mathbf{d}|h_b, \mathbf{n}))}{p(\mathbf{d}|0)}. \quad (2.36)$$

This statistic represents the maximum likelihood I can achieve under the hypothesis that there is a GW in the data. Thus, this energy is equal to the maximum energy in the scalar polarization. For a more complete treatment on this statistic,

also known as the standard likelihood statistic  $E_{SL}$ , as it is formulated in the GR frame, see [27]. Therefore, I can think of the null stream as simply the coherent energy leftover after the maximum energy consistent with a GW is subtracted out. The total coherent energy can be found by taking the dot product of the data with itself

$$E_{tot} = ||\mathbf{d}||^2 \quad (2.37)$$

Therefore, the null energy can be represented as

$$E_n = E_{tot} - E_{SL} = E_{tot} - E_b \quad (2.38)$$

$$= ||\mathbf{d}||^2 - \frac{\max(p(\mathbf{d}|h_b, \mathbf{n}))}{p(\mathbf{d}|0)} \quad (2.39)$$

$$= ||\mathbf{d}||^2 - ||\mathbf{e}^b \cdot \mathbf{d}||^2. \quad (2.40)$$

In other words, the null energy can be thought of as the minimum amount of energy in the data that is due to noise.

This nuanced way of looking at the null stream coherent energy can give us an idea on what side of the  $E - I$  line GWBs will fall when it comes to the incoherent and coherent null energy. The coherent null energy of a GWB will be very small as I have subtracted out the standard likelihood. Conversely, the incoherent energy will be large. Therefore, I anticipate that GWBs will fall to the left of this line, i.e.  $E_n \ll I_n$ . The loud noise, however, will tend to have similar coherent and incoherent null energy. This general analysis of the null energy can be applied to the coherent statistics involving the polarization energies themselves. For instance, I can project the scalar energy  $\mathbf{e}^b$  onto the data. Unlike the null energy case, I have constructed this statistics such that a scalar polarized signal should have a build up of coherent energy and end up to the right of the  $E - I$ , i.e.  $E_b \gg I_b$ . In general, loud noise in this statistic may look like a scalar signal in one detector, but will not look like a signal in the coherent energy. Therefore, it will fall on the  $E_b - I_b$  line. Fig. 2.1 demonstrates these two cuts.

### 2.3.3 Benchmarking Performance

Lacking from the discussion above is that choosing cut C requires the analysis to know how far from the  $E - I$  diagonal the GWB would fall. This is why the analysis also simulates signals and injects them into the on-source region, i.e. the time around the astrophysical event a GWB could have entered the data. Because the waveforms I simulate directly impact the choice of cut C, it is critical that I choose waveforms representative of potential signals from the astrophysical event. I discuss the choices of scalar waveform in Section 2.4 and choices made for GRBs are discussed in [11] and choices for CCSN are discussed in both [12] and Section 3.2. In addition, the potential for the background to have loud noise transients during the on-source period must be taken into account. Therefore, an identical analysis is performed on a large number of TF-maps from data surrounding the trigger time to characterize the noise in the detector. This data is referred to as the off-source data and is assumed to not possess a GWB.

The process for determining cut C is as follows. Initially, I divide the injected signals randomly into two groups, a tuning set and an upper limits set. In general, for N injected signals there tend to be N/2 injections for tuning and upper limits. I

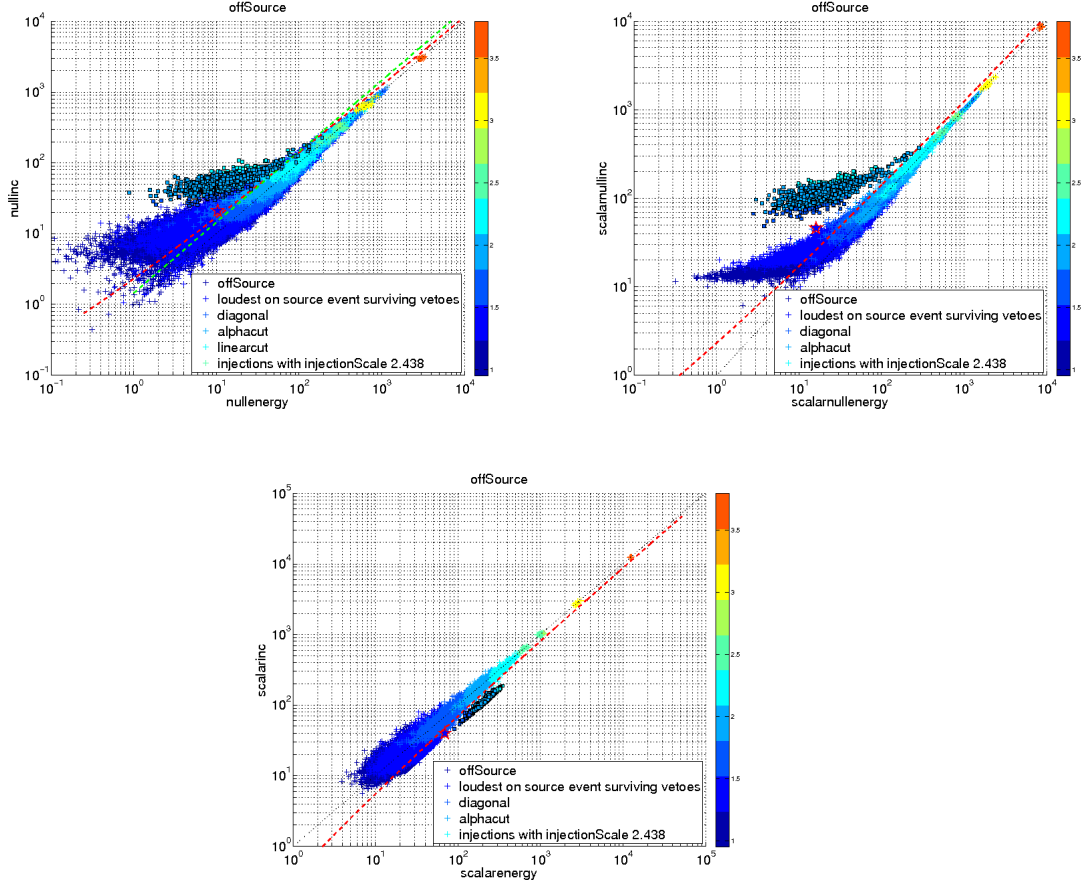


Figure 2.1: Graphs demonstrating the effectiveness of coherent consistency checks. Top-Left: Null Coherent by Null Incoherent Energy. The square plot points represent the simulated GWB signals which appear on the left side of the E-I line and the crosses represent the background noise. As you can see the dashed red cut line recovers most of signals, while eliminating most of the background. Top-Right: Null Scalar Coherent versus Null Scalar Incoherent. Because the scalar signal is a single polarization the scalar coherent statistics have an additional scalar specific null stream. As with the null energy, the GWBs appear on the left side of the E-I line. Bottom: Scalar Coherent by Scalar Incoherent Energy. Again, as expected the simulated GWB signals appear on the right side of the E-I line.

also break the off source trials into two sets, those used for tuning and those used for upper limits. Between the off-source and injection tuning sets, I test a set of linear cuts  $C_{Linear}$  and alpha cuts  $C_{alpha}$ . These two coherent cuts have different shapes. The linear cut compares the ratio of  $\frac{I}{E}$  to some threshold value. The alpha cut compares the value  $\frac{2(E-I)}{(E+I)^\alpha}$ , where the constant  $\alpha$  is 0.8. I choose  $C_{linear}$  as the threshold that most effectively recovers 95 percent of the tuning injections. In order for a tuning injection to be recovered, it must pass a given cut threshold and be louder than the loudest surviving tuning off-source event at some false alarm probability (FAP). This captures the quintessential balance with coherent cuts. The stronger the cuts the less significant the background will be, but the more injections that will also be discarded with a statistic designed to distinguish them from the

background. Conversely, the weaker the cuts the more injections that will pass, but the louder the background will be and the more likely the background will contain loud noise transients. The FAR relates to the selection of the loudest background in the following way. For  $N_{tuning}$  background trials, I select the loudest surviving event from each trial and then rank them in magnitude. I then take the  $FAP * N_{tuning}$  index event from this ranking, and subsequently the whole trial from which that event came from, as the fake on-source trial. For the analysis, the definition of “most effectively” is the cut that minimizes the sum squared fractional excess upper limit (SSFEUL) statistic. For waveforms  $w \in \Omega$ , the SSFEUL is defined as

$$\sum_w \left( \frac{I_{95} - \min(I_{95})}{\min(I_{95})} \right)^2 \quad (2.41)$$

where  $I_{95}$  is the injection scale or amplitude at which for all larger amplitudes 95 percent or greater of the tuning injections are recovered. After I pick a cut  $C_{Linear}$ , I choose  $C_{alpha}$  as the threshold that most effectively recovers 50 percent of the tuning injections after having the linear cut already applied. Finally, after the ranking statistic and coherent cuts have been selected, they are applied to the injections and background assigned for upper limits. It is the recovery of these injections that get plotted to make the efficiency curves. Therefore, upper limit statements made using these curves indicate that with some confidence I would be able to recover GWs that had the characteristics of the simulated signals.

Through the tuning and upper limits process above, I have only discussed upper limit curves in terms of some FAP off-source event. Of course, any signal from the astrophysical event would be in the part of the data called the on-source. The reason the background gets so much attention and testing is because once I look at events in the on-source window, then there is no point of return. In the case of SN waveforms, I provide an upper limits curve and produce a 90 percent confidence distance limit. The off source is used to select thresholds so that the tuning is not biased by any GW signal in the on-source data. This is called the “blind tuning” of the analysis. To decide if a GW is present, the most significant on-source event is compared to the off-source events to assign its FAR. If no significant on-source event is found, then limits on the amplitude of the signal can be placed. In this case, that statistic means that, in an ensemble of identical experiments (i.e. a SN exploding at the same distance and same spot every year), then the *true* distance to the source will be greater than the stated 90 percent distance limit for 90 percent of those experiments.

## 2.4 Benchmarking the Scalar Search

The analysis performed in this section considers the H1L1 and H1L1V1 detector configurations. I use data from the S5-VSR1 observing run rescaled to the expected 01 sensitivity. In order to provide a realistic idea of the detection sensitivity of the searches, I chose seven test waveform models and four test supernovae sky-locations with right ascension and declination angles of [284.0054 -52.4654], [298.9727 -41.4060], [309.3363 -28.9943], and [317.4038 -15.9633]. In the following subsections, I discuss the criteria behind the selected waveforms and sky locations.

### 2.4.1 Choice of Scalar Waveforms

The simulated waveforms I selected for the analysis are critical as they will impact what coherent cuts the pipeline chooses. Our three main criteria for the selection of scalar gravitational waveforms are as follows. First, I chose waveforms from a wide variety of astrophysical models that could produce scalar gravitational waves. Although this analysis is for a GS, it is unclear what scalar gravitational waveforms would look like and having a range of astrophysical models will assist in capturing that uncertainty. Second, I chose waveforms that had a wide range of scalar gravitational radiation energies, from the very optimistic to the pessimistic, because the strength of scalar waveforms is a subject of debate. Third, I want waveforms that span the frequency range from 64 to 2000 which is our planned Supernova frequency search range. This range is motivated by all of the possible GWs associated with a CCSN summarized here [37].

The first waveform was theorized by Nishizawa et al. [2], who modeled the gravitational collapse of a spherically symmetric dust fluid into a BH. This astrophysical phenomenon is similar to the gravitational collapse that occurs during a CCSN. Specifically, I utilized the A1 model from the paper which simulates the collapse of a 10 solar mass dust fluid at a distance of 10 Mpc. I performed modifications to the distance and mass of this model in order to achieve a diverse set of central frequency values for this waveform.

The second set of waveforms are simulations by Novak and Ibanez of scalar GWs associated with a CCSN and the subsequent formation of a neutron star [3]. This paper had 5 different SN models, labelled A-E, but only models C-E were scalar gravitational wave progenitors. These models all simulated a  $1.39 M_{\odot}$  white dwarf but differ in two characteristics. First, Models C and E use “standard” values for the equation-of-state parameters, but model D has a “stiff” equation-of-state value. Second, Model C and D are simulated assuming  $\alpha$  and  $\beta$  values of -0.01 and -4 respectively whereas Model E’s values are -0.001 and -7. For this reason, Model E is the most optimistic of the simulations possessing the most energy in the form gravitational radiation because large  $\beta$  values lead to large gravitational energy.

The third set of waveforms are simulations by Novak of a NS undergoing spontaneous scalarization [56] as well as a spherical collapse to a black hole [4]. For the first of these papers, an unstable NS transition to a strong-scalar-field state is explored. A NS can achieve this “spontaneous secularization” if  $\beta$  is low enough. In this analysis, I use the waveform from solution 4, which is a 1.37 solar mass NS that is 13.2 kilometers in diameter and  $\alpha$  and  $\beta$  values of -0.01 and -6, respectively. For the second of these two papers, Novak simulated four different types of NS collapse, labelled A-D. I utilize the waveform resulting from collapse B in this chapter. This collapse follows the collapse of a 2.07 solar mass NS that is 11.8 kilometers in diameter and  $\alpha$  and  $\beta$  values of -0.025 and -5, respectively.

The final waveform chosen was a scalar sine-Gaussian which serves as a standard proxy for a physical scalar waveform model. These models are useful as it is easy to manipulate the frequency of the signal. In addition, these are standard waveform templates used for bench-marking burst searches in LIGO and Virgo [11]. The frequency, scalar coupling parameter, and more information on all these waveforms is available in Table 2.1. Additionally, Figure 2.2 shows examples of some of these waveforms.

As discussed in the introduction, the constraints on the  $\alpha_0, \beta_0$  parameter space have tightened since the creation of these waveform models due to the solar system

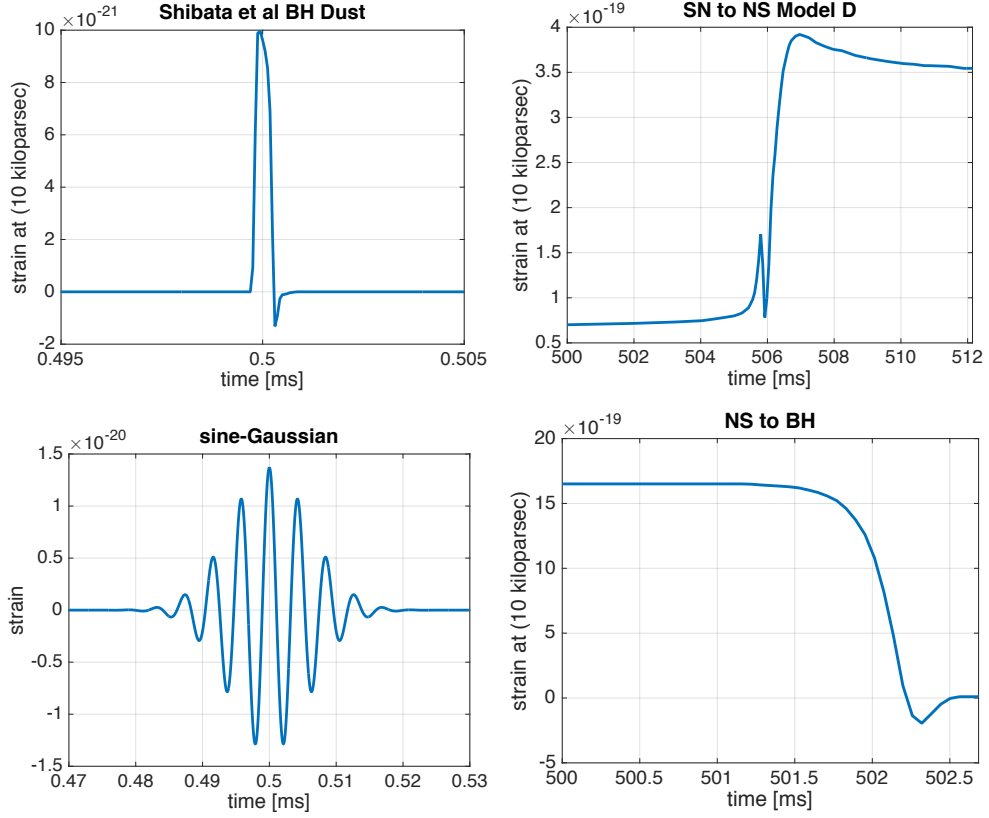


Figure 2.2: A selection of the scalar waveforms used in this analysis. The  $\alpha_0, \beta_0$  values are in parenthesis. Top-Left: Dust undergoing gravitational collapse to a BH ( $3.5 \times 10^{-3}, 0$ ) [2]. Top-Right: Model C CCSN explosion and subsequent formation of a NS, ( $4 \times 10^{-4}, -4$ ) [3]. Bottom-Left: sine-Gaussian waveform Bottom-Right: NS collapse to a BH, ( $0.025, -5$ ) [4].

experiments from the Cassini probe and those from the discovery of the white dwarf J1738+0333. The question becomes with the scalar models in this analysis what transformations can be performed to make these waveforms compliant with present constraints on the  $\alpha_0$  and  $\beta_0$  parameter space. In particular, I need to know how the amplitude of the waveform scales with respect to one or both of the parameters  $\alpha_0$  and  $\beta_0$ . This relationship is important because the amplitude is the only component of the waveform I can manipulate in the analysis.  $\beta_0$  cannot be altered because it will change the shape of GW, and thus, a complete rerun of the simulation would need to be performed. Fortunately, the amplitude scales directly with  $\alpha_0$  and changing this parameter does not change the shape of the waveform. In the Novak simulations, the amplitude relates to the parameters  $\alpha_0$ , distance and  $a^2(\phi_0)$ , which represents the scalar field at the source, as follows

$$h(t) = \frac{2}{d} a^2(\phi_0) \alpha_0 F(t). \quad (2.42)$$

In the Shibata paper, the peak amplitude roughly relates to the parameters  $\alpha_0$ , mass and distance as follows

$$\delta\phi \simeq \frac{\alpha_0 M}{d} \quad (2.43)$$

Source	Hz	Dist. (Kpc)	$\alpha_0(-1 \times 10^{-5})$	$\beta_0$	Mass ( $M_0$ )
Dust Collapse into BH [2]	183	15	350	0	5
	413	3	350		3
	781	1	160		1
	984	1	350		0.9
	1034	0.2	40		0.5
SN Models (C-E) [3]	163	10	40	-4	1.39
	126		40	-4	
	103		1	-7	
NS Spontaneous Scalarization [56]	147	10	1	-6	2
NS Collapse to BH [4]	120	10	40	-5	2.07

Table 2.1: This table lists my parameter choices for the waveforms and sources in this analysis. The parameters that were modified from their original values are the distance, the  $\alpha_0$  parameter and the mass.

In general, I only modified the  $\alpha_0$  parameter to the boundary of the constraint.

Unfortunately, three of our waveform models are no longer consistent with the viable  $\beta_0$  parameter space. But these models are meant to illustrate the method of detecting a scalar polarized signal, so I included them in the analysis with  $\alpha_0$  lowered to place these waveforms close to allow parameter space. Figure 2.3 details the degree to which I modified the  $\alpha_0$  in order to place these waveforms within the viable parameter space. Due to the weakness of the scalar signal, I believed that the plausibility of detecting the signal would rely on allowing for the largest possible values associated with the strength of the scalar field. For two Shibata injections, however, I changed  $\alpha_0$  such that it fell well below the largest allowable  $\alpha_0$  value. This was done in order to see if aLIGO could probe well below current constraints in the event new constraints were placed during its operation.

#### 2.4.2 Choice of Sky Location

There were three criteria for the simulated sky-location and alert or trigger time of our GS. First, I selected sky-locations that lined up with the location of the galactic disk on the sky for a given GPS time. In particular, one of the sky locations was the location of the galactic center. The choice of these sky-locations was in order to emulate the plausible location of a GS in case of a real alert. That is to say, the GS will likely come from the Galactic center or nearby. Second, the sky-location and trigger time maximized the detector sensitivity to the scalar polarization. Finally, I ensured that there was sufficient usable detector data surrounding the trigger time. Figure 2.4 demonstrates the antenna response of the detectors for the trigger and sky-locations I chose for this analysis.

There are two important things to note from these plots. First, there is a stark contrast in GR and scalar antenna response. I chose a time with very different responses to determine the potential magnitude of the effect of performing a GR-only search for a scalar signal. If there is little difference between the GR and scalar search in this case, it shows that a separate search for a scalar waveform associated with a GS is unnecessary. Second, there is one sky-location that has a poor detector sensitivity compared with the other three. This is in order to gauge the fall off in efficiency in the recovery of signals with the dedicated search when dealing with fringe sensitivity levels. Because the amplitude of scalar waveforms is expected to be



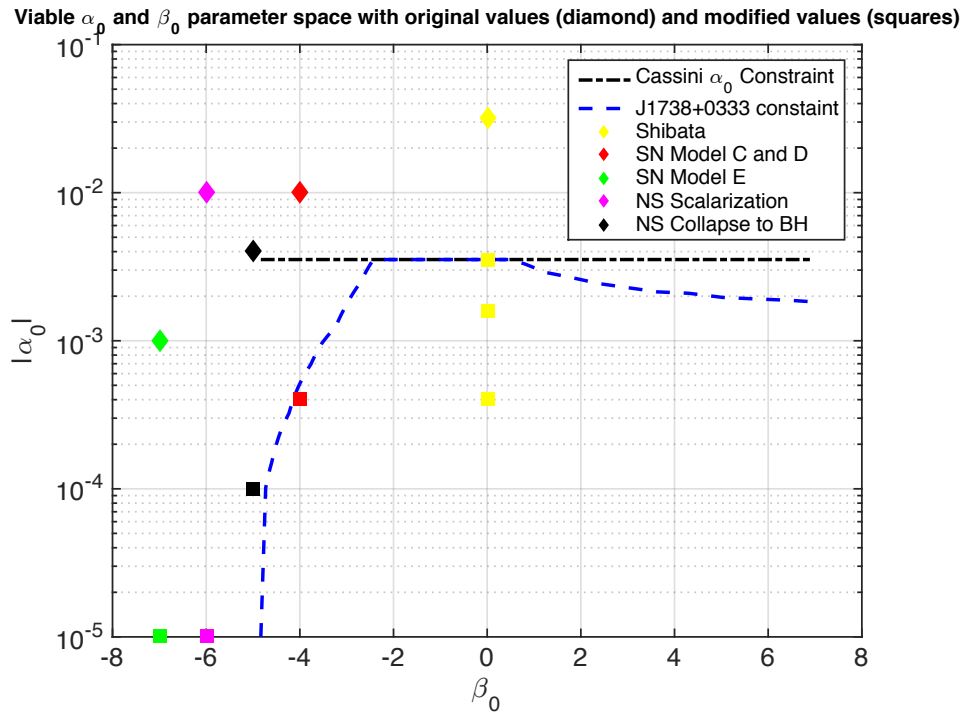


Figure 2.3: Current constraints on the  $\alpha_0, \beta_0$  parameter space. It is bounded by the Cassini probe experiments (under the black line) [5] and by the white dwarf J1738+0333 observations (under the blue line) [6]. The diamonds represent the original assumed values of  $\alpha_0$  and  $\beta_0$  for the various scalar waveforms considered and the squares are the new values used in the analysis done in this chapter.

small relative to the GR case, I anticipate not being able to recover the waveforms for this sky-location.

## 2.5 Galactic Search results

### 2.5.1 Upper Limits

In this section, I initially seek to answer whether scalar gravitational waves emitted at reasonable distances are detectable within the viable  $\alpha_0, \beta_0$  parameter space. Following this discussion, I explore more questions such as whether the addition of the statistics presented in this paper improve the sensitivity of the search over and above existing GR polarization statistics.

Figure 2.5 provides insight on the first question. This plot shows that a Shibata waveform with parameters  $2M_\odot, \alpha_0 = 0.0035$  and a Novak SN Model C waveform are detectable at distances of a few kpc. These two waveforms highlight models whose  $\alpha_0, \beta_0$  values were on the boundary of the viable parameter space.

Table 2.2 provides information on the 50 percent detection distance of all the waveforms average over the 4 sky locations for H1L1 and H1L1V1 detectors. I averaged over the sky locations because they roughly cover the minimum and maximum detector sensitivity. As expected, the waveforms whose  $\alpha_0$  fell well below the largest allowable value have detection distances less than 1 kpc. Also, those waveforms with  $\beta_0$  larger than current limits on  $\beta_0$ , i.e. NS collapse to BH and SN Model E, have

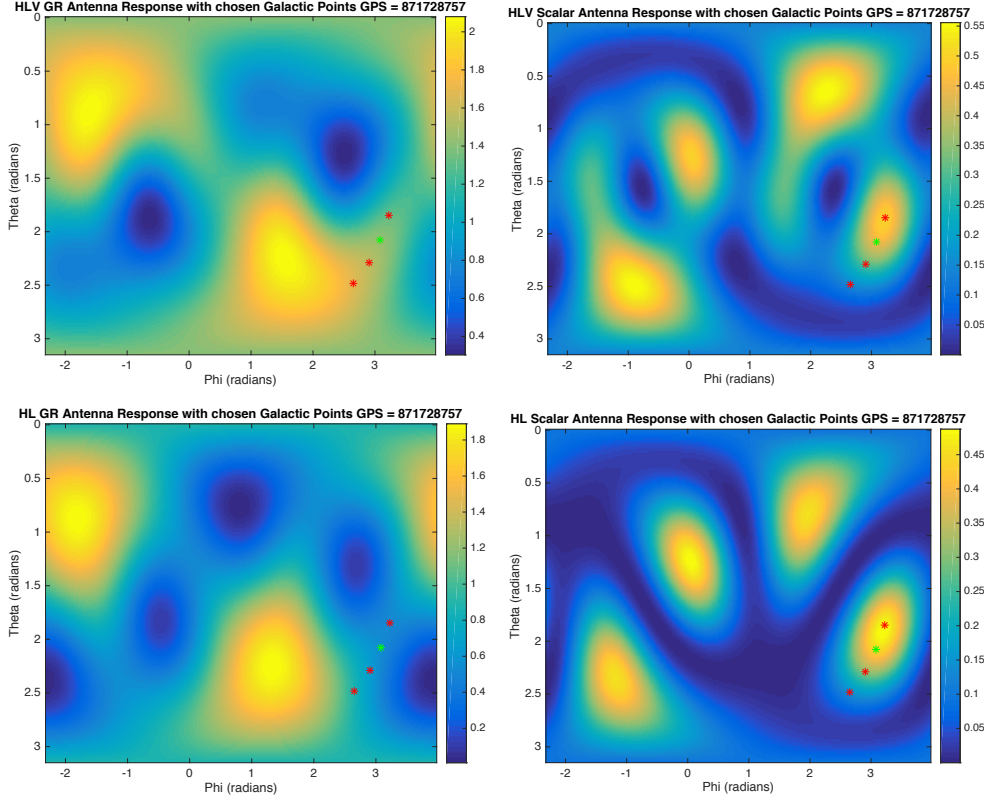


Figure 2.4: These plots show the antenna response for the GR ( $F_+^2 + F_\times^2$ ) and scalar polarizations ( $F_b^2$ ) over the whole sky summed over different detector configurations H1L1 and H1L1V1 at a GPS time of 871728757. Top-Left: Shows the plus/cross response for H1L1V1 detector configuration. Top-Right: Shows the scalar response for H1L1V1 detector configuration. Bottom-Left: Shows the scalar response for H1L1 detector configuration. Bottom-Right: Shows the plus/cross response for H1L1 detector configuration. The overlaid 'x' marks the locations of the four sky points considered in this chapter.

detection thresholds on the order of a few tens of kpc. Even though the  $\alpha_0$  value for these signals was small, scalar fields with large negative  $\beta_0$  values result in a large scalar signal. Additionally, Novak Model D has encouraging detection distances, but it is important to note that this simulation was done assuming a “stiff” equation of state and thus has a stiffer bounce. These results are still promising, as they imply that a GS can prove useful in either eliminating certain scalar waveform models, further constraining the  $\alpha_0$ ,  $\beta_0$  parameter space or constraining the equation of state of NS stars.

It appears that scalar mode signals with  $\alpha_0$  and  $\beta_0$  values allowed by current constraints are detectable at astrophysically relevant distances, i.e. kpc. The next step was to determine if a dedicated scalar search was necessary or if the standard GR search could detect these signals as efficiently. Therefore, I duplicated the analysis utilizing the preexisting coherent statistics, plus/cross, circular, and linear. Figure 2.6 highlights the results from this analysis. The sensitivity of the various searches across the waveforms and sky positions looked very similar. There are a few trends worth noting. The resulting efficiencies from the run on the sky position with the best plus/cross and worst scalar response overlapped more closely than those from

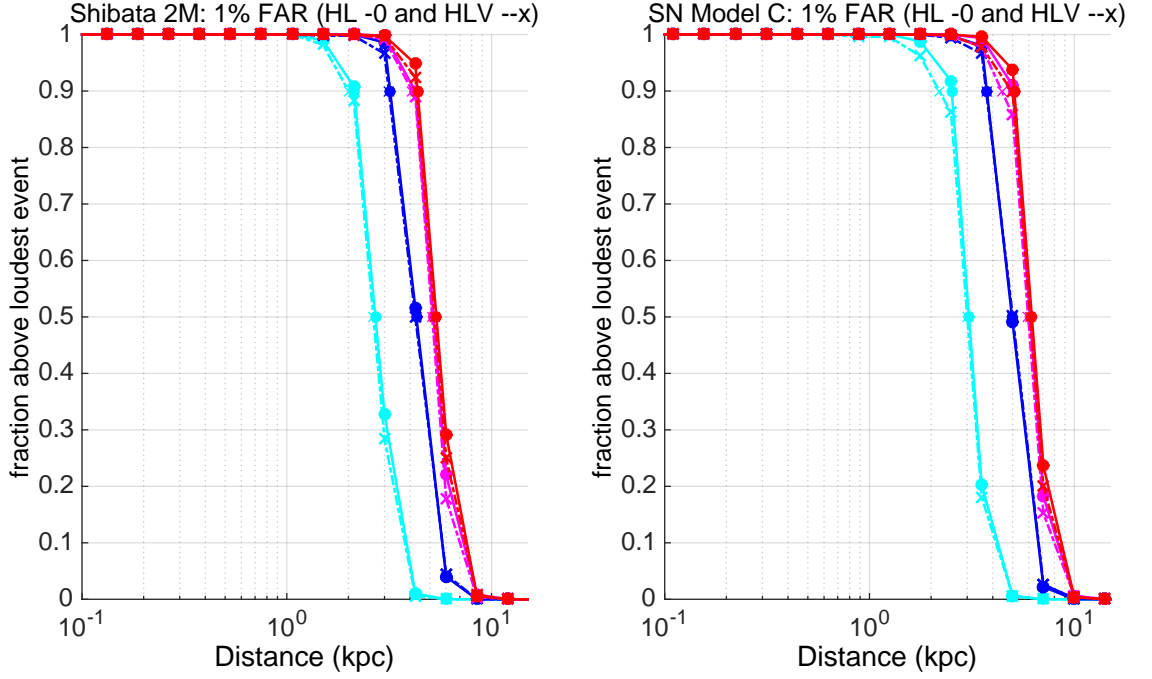


Figure 2.5: Efficiency for a 1% false alarm rate threshold for a dust collapse and SN waveform injection using the scalar statistics formulated in this chapter. The four curves represent the four sky locations with the least sensitive recovery (farthest left) coming from the smallest antenna response to the scalar polarization and the most sensitive curve (farthest right) coming from the sky locations with the best scalar polarization response. Both models utilize  $\alpha_0$  and  $\beta_0$  parameters that are valid but on the fringe of the parameter space as indicated in 2.3:  $(3.5 \times 10^{-3}, 0)$  and  $(4 \times 10^{-4}, -4)$ .

the sky location where the reverse was the case. Figure 2.6 exemplifies this trend. This difference in sensitivity, although visible, is negligible with systematic and statistical errors associated with this type of search. Another important insight from these follow up analyses is that the best performing ranking statistics chosen in every analysis was the scalar statistic formulated through Bayesian inference which was demonstrated in this chapter. Therefore, the small improvement that comes from utilizing scalar coherent cuts means a specialized scalar analysis is only necessary in cases where the GW is marginally detectable, i.e. the distance of the GS is slightly farther than these upper limit detection distances.

I attribute this result, the successful sensitivity of the standard statistics in the recovery of scalar signals, to the antenna response functions of the detector with respect to the scalar and plus/cross modes. It is possible that the cross/plus and scalar antenna response values are identical to within, say, 5 percent for a given polarization angle. Mathematically, this means that if there exists a polarization angle  $\psi$  and scale  $\lambda$  such that  $\mathbf{F}^b = \lambda \mathbf{F}^+(\psi)$  to within some accuracy then the scalar signal  $h_b$  would be indistinguishable from a GR signal with amplitude  $h_+ = \lambda h_b$ .  $\mathbf{F}^b$  and  $\mathbf{F}^+(\psi)$  are a vector of the individual detector responses as in Eq. 2.44.

$$\mathbf{F}^+(\psi) = \begin{bmatrix} F_H^+(\psi) \\ F_L^+(\psi) \end{bmatrix} \quad \mathbf{F}^b = \begin{bmatrix} F_H^b \\ F_L^b \end{bmatrix} \quad (2.44)$$

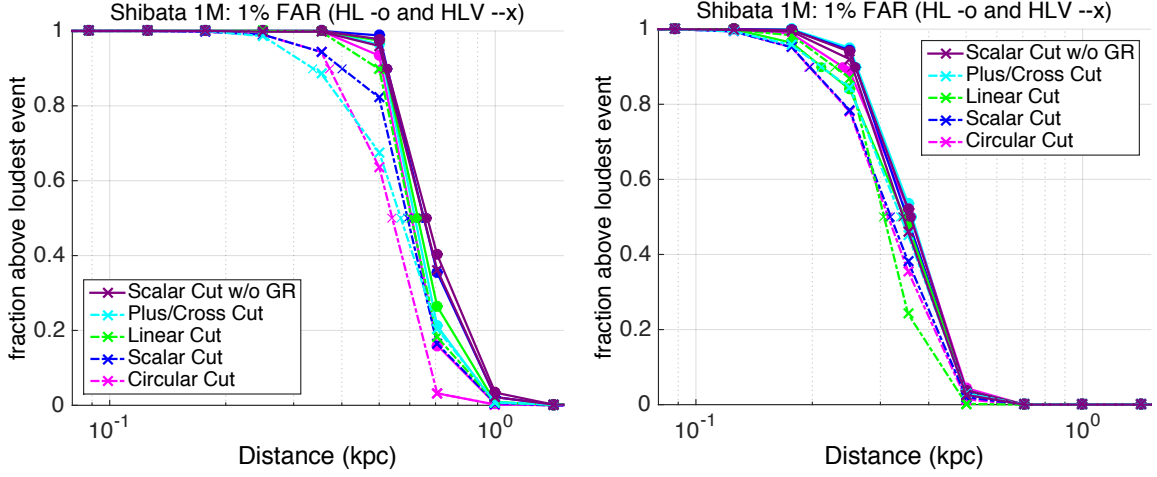


Figure 2.6: Comparing detection efficiency of the scalar-mode search with that of the GR-mode search. For region of sky tested, see that scalar GWs are picked up by the GR search about as well as by dedicated scalar search. Yet, for the sky position with the best GR detector sensitivity compared with the scalar sensitivity (right plot) the distinction is even harder to make between the searches than the analysis where the opposite was the case (left plot). That is, the scalar sensitive was the best compared with the GR sensitivity.

Therefore, I calculated the antenna responses for a grid of sky positions to see for which sky points there were distinctive values for scalar and plus/cross antenna response. To do this, I rotated the polarization angle for each sky point from  $[0, 2\pi]$ . Figure 2.7 shows that this degeneracy is highly likely in the case of two detectors. All of the sky locations which coincide with distinctive antenna responses to the scalar versus plus/cross polarization are also associated with extremely poor sensitivity values.

Another result that deserves more exploration is the fact that adding the third detector data stream, in this case Virgo, either does not affect or decreases sensitivity to scalar signals. This result is curious as the results should at least scale upwards proportional to the sensitivity of the third detector. I believe the reason for this odd result is twofold. First, the data from the Virgo detector is less Gaussian, i.e. more "glitchy", than the data from the LIGO detectors, Hanford and Livingston, see Figure 2.8. This fact within itself would not inherently lead to poorer sensitivity. Therefore, the second reason is that the sensitivity of the Virgo to the scalar polarization is low for all these sky locations ( $< 0.1$ ), and this means the addition of the Virgo data stream is mostly only adding background noise some of which is much louder than the Hanford and Livingston data. Although I would anticipate that a better detector sensitive to the scalar mode coupled with less noisy data would improve the sensitivity of a specialized scalar search, it is unlikely that the scalar statistics would have an impact even in this scenario. This is because the addition of a sensitive third data stream is equivalent to the addition of a powerful null stream of data. As discussed in Section 2.3, this data stream is helpful in the detection of a GWB, but does not rely on any assumptions of the polarization of the signal. Thus, the standard statistics would likely provide identical results to the scalar statistics.

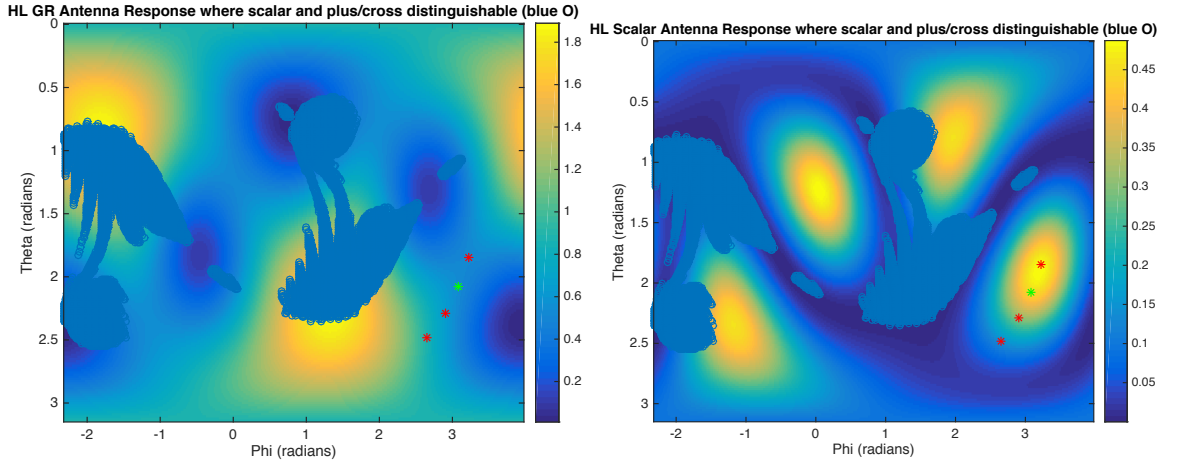


Figure 2.7: Left: HL antenna response overlapped with a scatter plot of sky positions where the scalar and plus/cross polarization are distinguishable in value by more than 5 percent. Right: Same as left except with scalar antenna response. This figure highlights an unfortunate caveat when searching for a scalar signal with specialized statistics, the sky locations where the polarization are distinguishable are associated with extremely poor sensitivity to the scalar polarization.

## 2.6 Conclusion

It appears that even with constraints that are presently acceptable in scalar tensor theories, there is some hope at certain distances ranging from a few kpc to more than 10 kpc that one could detect a scalar waveform. However, it seems that a dedicated scalar follow up is only useful if the following conditions are present. First, the sky location is in an area where there is no degeneracy between the plus/cross and the scalar antenna response. Second, the sky location is in an area where there is a fairly strong scalar antenna response. Third, in the case of three detectors, if null stream data proves a source of a powerful coherent cut then the assumption of the polarization of the signal could prove unhelpful and the dedicated statistics would lose some of their value.

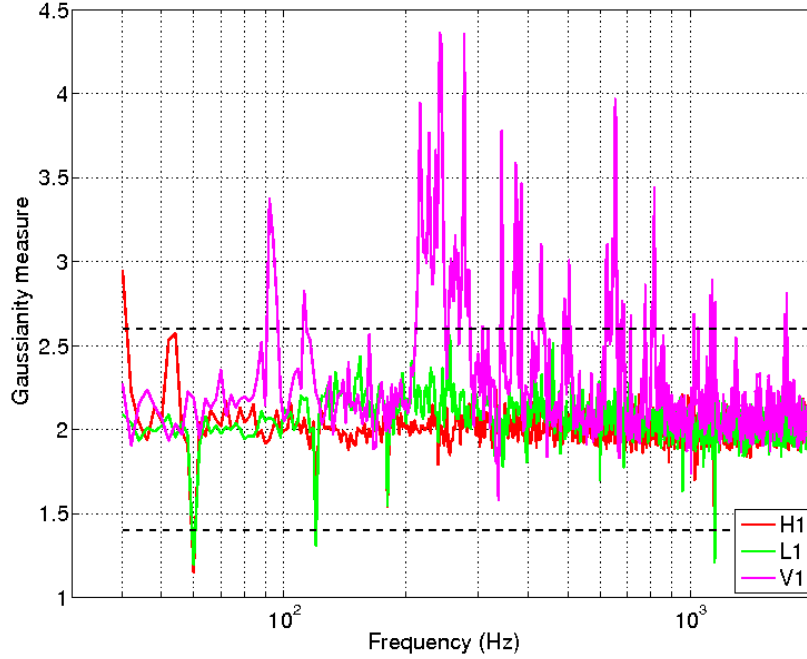


Figure 2.8: Plot depicting ”glitchiness” of the data. The Gaussianity measure is the  $\frac{\text{variance}(S)}{\text{mean}(S)}$  in each frequency bin where  $S$  is the one-sided noise power. A value of 2 is expected for stationary Gaussian noise. The dotted lines indicate 3-sigma variations. Excursions to large values indicate the data is more variable than expected for Gaussian noise, i.e. ”glitchy”. Excursions to low values indicate low variability. The green and red dips to low values are due to large steady values of power that are associated with known events such as the 60Hz power lines.

Source	50% Dist. (kpc) HL	50% Dist. (kpc) HLV
Dust Collapse into BH [2]	19.3	19.1
	4.3	4.3
	1	1
	0.55	0.55
	0.04	0.04
SN Models (C-E) [3]	5.0	5.0
	26.9	26.4
	33.8*	30.8*
NS Spontaneous Scalarization [56]	5.1*	4.7*
NS Collapse to BH [4]	28.2*	29.7*

Table 2.2: This table lists the 50% detection efficiency distance at a false alarm rate of 1%. The values are derived from an equal weighted average across the four sky locations in our analysis. The detection distances for the waveforms with very large  $\beta_0$  are due to the large amplitudes associated with models that assume  $\beta_0 \neq 0$ . The asterisk indicates a waveform model whose  $\beta_0$  value falls outside current constraints.

## Chapter 3

# Supernova Early Warning System Online Search

In Chapter 2, I discussed the potential of a GS occurring. The rate of GS is uncertain and can range widely, but estimates roughly average a maximum of 1 every 30 years [57]. This means a GWB search for a GS should be ready to automatically follow-up an alert and send information to the larger astrophysical community as quickly as possible, to maximize the scientific exploitation of these events. The community in charge of the initial alert of a GS is the SuperNova Early Warning System (SNEWS). The current members of the SNEWS experiment include Super Kamiokande (Super-K) [41], the Large Volume Detector (LVD) [58], IceCube [59], Borexino [60], Daya Bay [61], and KamLAND [62]. The Sudbury Neutrino Observatory (SNO) [63] is also a member but is currently undergoing upgrades. The majority of these detectors were designed for other purposes than strictly the detection of GS neutrinos, but all are capable of serving this purpose. In this chapter, I will discuss the current implementation of the low latency, quick turnaround, online search that would follow from a SNEWS alert. I first introduced the X-Pipeline algorithm in Chapter 2, in order to motivate the analysis done in this chapter. In general, a search of detector data upon a receipt of a GS alert has two crucial components, speed and accuracy. Therefore, this chapter highlights techniques and benchmarking done to improve both components.

In Section 3.1, I describe how SNEWS works, and why neutrinos provide ideal external triggers for GWB searches. In Section 3.2, I detail the SN waveforms used in this analysis. In Section 3.3, I discuss the challenges involved in an all-sky triggered versus optically triggered GWB search. In Section 3.4, I present sensitivity estimates for both the all-sky and optical search using recolored initial detector data. In Section 3.5, I discuss future work that would be useful for further improving this analysis.

### 3.1 Neutrino Detection of a Galactic Supernova

In this section, I will briefly discuss the method for detecting neutrinos from Supernovae, why neutrinos provide excellent external trigger timestamps, and how the alert is distributed to the astrophysical community.

The detection of neutrinos has two components. First, the actual detection of a sufficient number of neutrinos to assure the source is a GS, and second, any information on the source direction obtainable by the detection. Neutrinos undergo

neutrino-electron scattering and the detectors can measure if the energy of the recoil electrons,  $T_{act}$ , in the detector exceeds some experimental threshold  $T_{exp}$ , which is different for each detector. For an example of how this happens in practice, I will summarize the process used by Super-K. Super-K analyzes data in two minute chunks. It searches for clusters of neutrinos, in time windows varying from half a second to ten seconds. If pre-defined thresholds are exceeded in any of these clustering windows, then noise reduction algorithms are applied to these clusters. After this noise reduction, the candidate clusters undergo stricter thresholds. For clusters that surpass this secondary threshold, the mean time between clusters is calculated. The motivation for this calculation is that clusters with small mean times are unlikely to be astrophysical in nature. When 100 cluster events have sufficiently large mean times and pass both thresholds, then staff members on site are alerted of a possible supernova candidate. Like GWB searches, the threshold is set at some FAR to ensure that the candidate event is not simply a “loud” background event. Also like the GWB search, it is difficult to confirm a detection with a single detector. Therein lies the motivation for SNEWS, which would confirm a detection through coincident neutrino detections among all detectors. This has the opportunity to reduce the FAR to less than 1 per century, which would be critical given the rare nature and importance of a GS.

Neutrino detectors can achieve pointing information one of two ways. First, detectors can utilize the scattering angle of the neutrinos to extract the direction from which they came. Second, a group of neutrino detectors, like those in SNEWS, can employ a technique called triangulation. This takes the timing of neutrino detection from several detectors and attempts to triangulate the source. Both of these techniques, especially the latter, present a number of challenges which are discussed in [64]. Nonetheless, any sky location information would be valuable not only to optical astronomers, but also in assisting the GWB search. In Section 3.3, I highlight the advantages of sky location information for the X-Pipeline analysis. Regardless, any sky location information would be unavailable with the first SNEWS alert. Therefore, it is necessary to prepare a GW search which would utilize no sky location information.

While the sky location information may be poor, the timestamp provided by SNEWS is both accurate and valuable for a GWB search. CCSN most likely emit GWBs either during the collapse or during the explosion over the next few seconds following the collapse. Recent simulations show that the time of the bounce and the maximum amplitude of the GWB from a CCSN have a strong correlation. Simulations also show that the time of the bounce is correlated with the onset of neutrino luminosity [65]. The question is, within what margin of error can the time of the first neutrino detection from the CCSN bound the time of the core bounce, and consequently, the time of the largest GWB. In a study by Pagliaroli et al, [65], the timing of the first neutrino detection and the core bounce is on the order of milliseconds. This means we can comfortably place a window of plus or minus 2 minutes around the neutrino alert and know that it would contain the GWB from the core bounce. The reason for the larger than necessary window is that other processes before and after the core bounce may also create GWBs [37].

To understand the impact of this narrow time window on the search, it is useful to compare with the time windows provided for more distant CCSN. Electromagnetic observations provide these time windows. These observations, however, typically only localize the time of GW signal to a 10 - 100 hour on-source region. The main



causes of this large window is observation cadence. That is, when a SN is observed, the window can only be constrained to the last time that portion of the sky was observed by a telescope. There are two key advantages to this small time window. First, the background, i.e. detector noise, around the event is easier to understand. In the case of a neutrino trigger, the analysis employs the same 3 hour background estimation that the GRB search utilizes. This 3 hour background helps ensure that the detectors are operating under similar sensitivity levels for both off-source and on-source trials. More importantly, this 3 hour background means there are fewer background noise events than for 10+ hours. The fewer background events means lower amplitudes of GWs can be detected. Third, the computational cost involved in a search of 4 minutes of on source data and 3 hours of background data with the goal of a 3-sigma detection is far less than a search with 10-100 hours of on source data. Follow-up analysis, if shown necessary, will be easier to conduct than follow-up analysis to EM triggered CCSN.

SNEWS will publicize two types of alerts, GOLD and SILVER. A SILVER alert requires manual on-site follow-up of the candidate event. On the other hand, a GOLD alert will be automatically sent to the astronomical community at large with the following information; the UTC time of the coincidence, all detectors involved in the coincidence and the type of alert. There are three criteria for a GOLD alert, and all criteria are in order to avoid a false alert. First, there must be at least 2 coincident detections within 10 seconds from two physically separated experiments. Second, at least two of the alarms from the individual detectors are tagged as GOOD. Finally, the detectors signifying a GOOD alert must have had consistent rates of GOOD detection candidates leading up to the coincident detection. A rate of GOOD alerts that is considered consistent is on the order of 1 per week. In the instance of a GOLD alert, an online GW event catalog system called GraceDB will receive and parse the information. This information will be used to set-up and automatically launch an X-Pipeline analysis. If more information such as sky location is available in a later alert, then a follow-up analysis of the event will be performed.

### 3.2 Discussion of Supernova Waveforms

In this section, I discuss the characteristics of the SN waveforms utilized in this study. As with the scalar waveforms, the selection of a diverse and comprehensive set of waveforms is important in the benchmarking of the analysis. Previous work shows that standard sine-Gaussian waveform templates like those used in GRB searches are not sufficient for the tuning of an analysis pipeline for a supernova. For example, the diversity of theorized explosion mechanisms of SN provide a wider range of signal morphologies than simple sine-Gaussians can capture. In addition, because of the near spherically symmetric geometry of a CCSN the GW signal may be linearly polarized. Therefore, numerical simulations of SN provide much better test waveforms for the search. Moreover, using waveforms from numerical simulations will allow for meaningful upper limits on the strength of GWs from SN as well as the elimination of theorized explosion mechanisms in the event of a non-detection.

The characteristics such as duration, frequency content, and polarization as well as its overall amplitude of a CCSN GWB depend on multiple factors including the dominant emission process and the complex structure, rotation, and thermodynamics of the progenitor star. Unlike CBC signals, it is impossible to robustly predict the signal's detailed time series because the CCSN explosion is necessarily messy

Waveform Type	Ref.	Model Name	$h_{\text{rss}}$ [ $10^{-22}$ @10 kpc]	$f_{\text{peak}}$ [Hz]	$E_{\text{GW}}$ [ $10^{-8} M_{\odot} c^2$ ]	Polarizations
Rotating Core Collapse	[9]	Dim-s15A2O05ls	1.052	774	$7.686 \times 10^{-1}$	+
Rotating Core Collapse	[9]	Dim-s15A2O09ls	1.795	753	2.630	+
Rotating Core Collapse	[9]	Dim-s15A3O15ls	2.692	237	$2.783 \times 10^{-1}$	+
Rotating Core Collapse	[10]	Sch-R1E1CA-L				+, ×
Rotating Core Collapse	[10]	Sch-R3E1AC-L				+, ×
Rotating Core Collapse	[10]	Sch-R4E1FC-L				+, ×
3D Convection	[8]	Müller-L15-3	$1.273 \times 10^{-2}$	144	$2.20 \times 10^{-3}$	+, ×
3D Convection	[8]	Müller-N20-2	$1.480 \times 10^{-2}$	175	$1.11 \times 10^{-3}$	+, ×
3D Convection	[8]	Müller-W15-4	$1.531 \times 10^{-2}$	204	$2.52 \times 10^{-3}$	+, ×
3D Convection	[7]	Ott-s27				+, ×

Table 3.1: This table is taken from [12]. From left to right it provides the physical mechanism, literature reference, model name, the root sum square gravitational wave strain ( $h_{\text{rss}}$ ), the peak frequency of gravitational wave emission ( $f_{\text{peak}}$ ), the total energy emitted in gravitational waves ( $E_{\text{GW}}$ ) and polarizations for the numerical waveform injections utilized in this chapter.

not unlike the merger and ringdown of a CBC signal. Even if the CCSN explosion mechanism was known and understood beforehand, this issue would still persist on account of this randomness. This fact is the key to understanding the bayesian ranking statistic versus the matched-filter statistic. Because the match-filter method relies on a theoretical prediction of the detailed wave signal (either of its time series or spectrum and phase), it is unhelpful to think of detecting a GW from a SN in this manner. As discussed before, the Bayesian statistic does not rely on any template information which is why it is a powerful and useful tool in here and in all burst searches.

This analysis uses waveforms from two types of CCSN mechanisms. These waveforms are a subset of those used in Gossan et al. [12]. The first GWBs are those from neutrino driven convection. In this type of explosion, the progenitor is non-rotating. This theory says that the stalled explosion is re-energized from neutrino heating. From among other things, GWBs form from the core bounce, prompt and neutrino-driven convection, and aspherical neutrino emission. In the search, I considered 3D simulations from Ott [7] and Mueller [8]. 2D simulations result in only one polarization, the plus, whereas the 3D simulations will have both plus and cross polarizations. The second type of explosion considered is that resulting from rotating core-collapse SN. In this case, the progenitor is rotating, which accounts for roughly 1 percent of all galactic CCSN. A strong GWB from pressure-dominated core-bounce will result from the core-collapse of a rotating progenitor. In this search, I consider simulations from Dimmelmeier (2D) [9] and Scheidegger (3D with magnetic fields) [10]. All of the rotating core-collapse models are based on  $15M_{\odot}$  progenitor with the LS180 equation of state and parameterized rotation profile. Table 3.1 summarizes useful information about these waveforms and Figure 3.1 shows what some of these waveforms look like. In the following results sections, I will present results from both 2D and 3D simulations as well as the two types of explosion mechanisms.

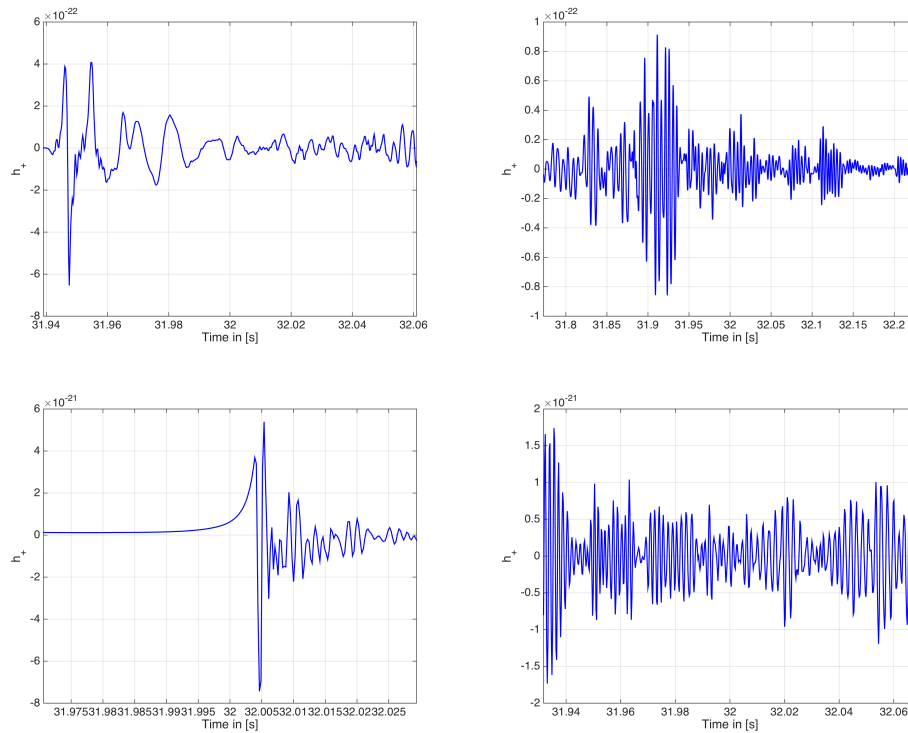


Figure 3.1: A selection of the SN waveforms used in this analysis. Top-Left: Waveform from a 3D simulation of neutrino driven convection explosion mechanism from Ott [7]. Top-Right: Waveform from a 3D simulation of neutrino driven convection explosion mechanism from Mueller [8]. Bottom-Left: Waveform from a 2D simulation of a rotating CCSN from Dimmelmeier [9]. Bottom-Right: Waveform from a 3D simulation of a rotating CCSN from Scheidegger [10].

### 3.3 SNEWS Triggered All-Sky vs. Optically Triggered Search

In this section, I describe the difference between a SNEWS triggered all-sky search and an optically triggered analysis. The difference between these two searches is that a SNEWS or neutrino trigger gives no sky position information whereas an optical trigger would contain the precise sky position of the SN. The motivation behind the setup for the all-sky search is the same as the optical. In the optical case, the time delay between the detectors is known from the sky location and thus the search can coherently combine the individual detector data streams without potential loss of signal. In the all-sky case, there is an infinite number of possible time delays for the Hanford, Livingston detector configuration. Therefore, in order to ensure the entire recovery of the signal, it would be necessary to search over all possible sky locations. This analysis is, however, computationally inefficient and the analysis with X-Pipeline would take too long. The key to constructing the all-sky search is creating a dense enough grid of sky locations that will sufficiently cover the full range of possible time delays. In [66], by J. Aasi et al. it is shown that using a linear grid of sky positions was sufficient to detect GWBs in GRB searches with sky areas of several hundred degrees. In this chapter, I extend the idea to an all-sky search and evaluate its effectiveness. Specifically, the grid must be dense enough so one or

more of the grid points will recover at least 90% of the SNR of the signal. In order to accomplish this, I chose a time delay between grid points of 0.1 milliseconds. To see why, imagine the worst case scenario of this grid of sky locations. This scenario would occur if the actual time delay was represented by a sky location halfway between two of the grid points. To see how 90 percent of the SNR would still be recovered, imagine a sine-Gaussian waveform. A sine-Gaussian waveform coming from this location would be maximally out of phase of a sine-Gaussian coming from either of the two grid points around it. The timing error of this sine-Gaussian would be 0.05 milliseconds. The SNR loss from this phase shift can be quantified as

$$SNR^2 = \cos(2\pi f_{signal} t_{err}) \times SNR_{max}^2 \quad (3.1)$$

where  $t_{err}$  is the timing error in seconds and  $SNR_{max}^2$  is the SNR from a sine-Gaussian at one of the two nearby grid points. In this analysis, the search looks for signals up to 2 kHz. Therefore, if this extreme situation is considered, that is  $f_{signal} = 2000$  Hz and  $t_{err} = 0.00005$  seconds, then

$$\begin{aligned} SNR^2 &= \cos(2\pi f_{signal} t_{err}) \times SNR_{max}^2 \\ SNR^2 &= \cos(0.2\pi) \times SNR_{max}^2 = 0.81 \times SNR_{max}^2 \\ SNR &= 0.9 \times SNR_{max} \end{aligned} \quad (3.2)$$

Thus, with this grid spacing, even in the worst case scenario, i.e. maximal frequency signal coming from a sky location whose time delay is represented by a point half way between two grid points, the recovery of the signal is still at roughly 90 percent. Next, it is necessary to determine the appropriate number of sky locations based on the time delay selection of 0.1 milliseconds. The time delay of a GWB between Hanford and Livingston is 10 milliseconds and the maximal timing error is 0.05 milliseconds. Thus, by simply dividing the two numbers, the search must be conducted on 201 sky locations. Figure 3.2 helps visualize this search grid. In addition, we added the galactic disk to the picture to demonstrate how the sky location steps line up with the galactic disk (which is where a GS would most likely occur.)

In this analysis, I ran with the same GPS time of 871728757 and on the same rescaled data as the analysis performed in Chapter 2. I test two cases, a SNEWS triggered linear grid search and an optically triggered, i.e. single grid point, search. I tested only the H1L1 configuration as this configuration is what is expected to be operational in late 2015 to early 2016. The right ascension and declination of the optically triggered analysis is [256.0009, -41.4060]. This point was selected as it lies in the galactic plane and is near the galactic center, [266.3644 -28.9943].

Because the validity of the coherent statistics formulated in the previous chapter relied on prior knowledge of the sky location of the source, the all-sky search provides some challenges for these statistics. First, the large range of time delays tested by the search will lead to much louder background than the optically triggered search. This is because there are more opportunities for background glitches in the detectors to appear in coincidence. In this analysis, the GR search statistics as formulated in [11] for the loudest background in the linear grid search was roughly 8000 whereas it was 5000 for the optical analysis. Moreover, no coherent cuts were selected by the post-processing of the output of the linear-grid search. This means none of the loud background events were eliminated by the post-processing and therefore all

HL GR Antenna Response with Half Galactic Disk and Linear Grid GPS = 871728757

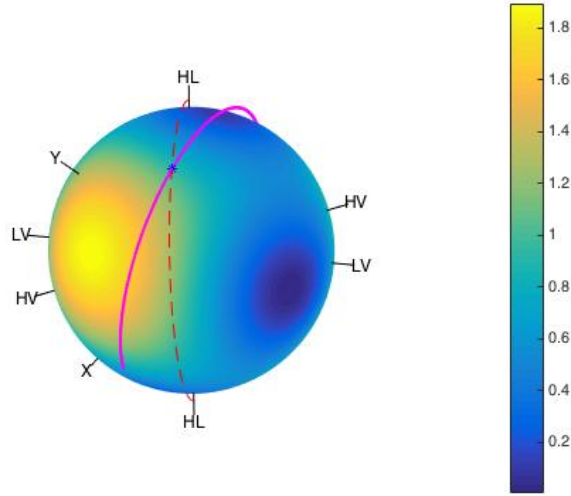


Figure 3.2: This figure shows the summed antenna response to the plus and cross polarization of Hanford and Livingston ( $F_+^2 + F_x^2$ ) overlaid with the linear search grid used in this search (dashed line). The solid line is the location of the Galactic Disk on the sky at this GPS time. The blue star at the intersection of the two lines represents the Galactic Center and is near the sky location used in benchmarking this search.

these events, including the event with a value of 8000, were still viable threshold candidates. In the optically triggered search, however, the loudest background post coherent cuts was around 38. The drastic reduction in background noise provided by the optical search over the linear grid search highlights issues inherent with the all-sky search. Figure 3.3 demonstrates the background issues in the triggered all-sky versus optically triggered analysis.

These plots raise the question as to why the loud background is not being vetoed out in the all-sky search to look more like the background in the optical search. The motivation for the coherent statistics was that the GWBs would separate themselves from the background, especially the “loud” background, and allow cuts to be made on the data. Without any sky location knowledge, however, all sky locations must be tested and some of these sky locations will cause a handful of the injected values to have qualities similar to the background. Figure 3.4 highlights these challenges.

Many of the injections fall away from the diagonal as expected, but a sufficient amount fall either on the E-I line or on the side of E-I line which is unexpected for a GWB. This is most likely because the antenna response at the grid points searched is not similar enough to the antenna response at the actual SN location, and so the coherent analysis fails. Because a nontrivial number of injections behave this way, no cut is selected for the linear grid search. As expected, the combination of the increased significance of the background in general combined with no cut selections causes the significance threshold at a FAR of 0.1 percent to be significantly larger than it is for the optical. This leads to poorer than expected efficient curves for the linear grid case. Figure 3.5 compares the linear versus optical efficiency curves at the 0.1 FAR for four different SN waveforms. The linear grid search loses an order of magnitude in recovery. Also, the linear, GR, and circular cuts display identical efficiency curves in the linear grid case because no cuts were selected on any of the

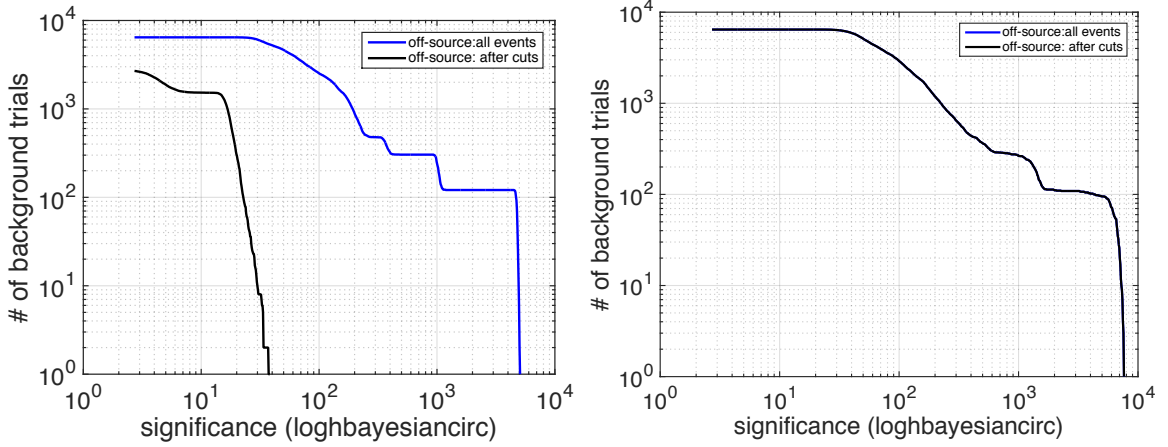


Figure 3.3: Left: The distribution of the significance (detection statistic), or “loudness”, of the background for the optical search using the loghbayesiancirc statistic [11]. The black line represents the entire background before any coherent consistency cuts are made and the blue represents the surviving background. Right: Same as the left except for the linear grid search. There is no blue line in this case as no cuts were selected, so the blue and black lines are identical.

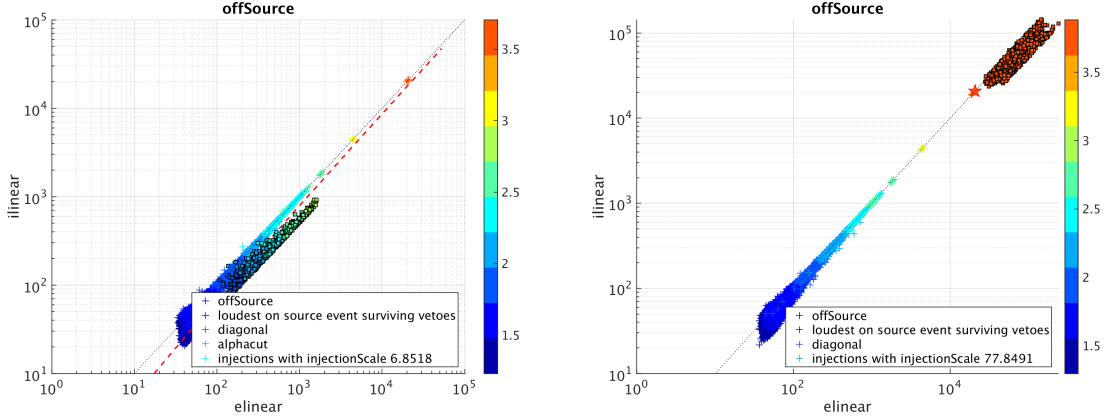


Figure 3.4: Left: Coherent versus Incoherent linear energy of the Ott 3D waveforms [7] in the optical search for the injection amplitude for which 90 percent of the injections were detected. The signals lie clear to the right of the E-I line and allow for an effective coherent cut selection. Right: Same as the left except for the linear grid search. This time a nontrivial number of the recovered signals energies lie on or on the opposite side of the E-I line. Although there are a number of injections whose statistics follow the expectation of the optical search, there are not enough in order to trigger a cut selection from the search.

post processing. These results appear discouraging at first glance, but information from the coherent versus incoherent plots such as Figure 3.3 provides evidence for a different approach. The background looks no different in the linear versus optical analysis in terms of where it falls on the E-I line. It is only the injections which falter. This implies it would be useful to force the cuts selected by the optical analysis onto the linear grid analysis. It is likely that the efficiency curves for the linear search will

never reach 100 percent but it seems probable that the 50 percent recovery would be nearly identical. The risk involved in accidentally cutting a GRB by employing these cuts as opposed to the cuts selected through X-Pipeline, is mitigated by the fact that follow-up analysis will also occur when better sky-location information is available. Therefore, it is useful to obtain the best possible 50 percent change at signal recovery at the initial alert than run an analysis that is unlikely to detect anything due to “loud” background. The results of this analysis are discussed in the next Section.

### 3.4 SNEWS Benchmarking

In this section, I seek to answer the following questions. First, in either the optically triggered or SNEWS triggered all-sky analysis, do any of the coherent statistics provide a significant improvement in the recovery of the signals. Second, how do the optical and linear grid efficiencies compare when employing the cuts selected by the optical post-processing on the linear grid search. Third, what potential solutions to the linear-grid search could be employed to fix the poor detection efficiencies. With the two detector configuration of Hanford and Livingston, it appears clear that there is no significant difference between using the circular, GR, or linear cuts. This result was not surprising as Hanford and Livingston are essentially aligned detectors and distinguishing polarization in the two detectors is challenging. Table 3.2 shows the 50 percent detection distance for the three cut types for all of the waveforms in this study for the optical analysis. Although the results are similar, the circular cuts provided the best 50 percent recovery in 9 out of the 10 waveforms. The X-Pipeline GRB search uses the circular statistics and they have shown to be effective at eliminating background [11]. In addition, for all the coherent cut types, either the loghbayesian [27] or loghbayesiancirc [11] were selected as the ranking statistic. This information suggests the use of only the circular statistics, and perhaps the plus/cross, is robust to effective recovery of these signals. This information will help reduce computational and time costs associated with the actual SNEWS search. This is because there is a nontrivial time involved in calculating the linear coherent statistics compared to the plus/cross and circular statistics. On average, three sky positions without the linear statistics can be analyzed in the same amount of time as one sky position with the linear statistics. Given the size of the grid in this analysis, this leads to nontrivial time increases, especially when doing enough background trials to achieve a 3-sigma detection.

A similar comparison of the coherent cuts in the linear grid search would prove unhelpful as no coherent cuts were selected by any of the post processing. Therefore, the circular, GR, and linear analyses are all identical as no background events were eliminated. If the coherent cuts selected in the optical analysis are applied to the linear grid results, then better than 50 percent detection efficiency are achieved for some waveforms, but for others the cuts are too extreme and eliminate over half of the simulated injection, even at high amplitudes. Unfortunately, this idea failed to deliver the desired result.

In addition to forcing some amount of coherent cuts on the linear grid results, information on the likely location of the GS can also help improve the analysis. As the name would suggest, a GS would come from the Milky Way Galaxy. The Milky Way’s location on the sky at any given GPS time can be calculated and the overlap between these sky locations and the time delay between the Hanford and Livingston

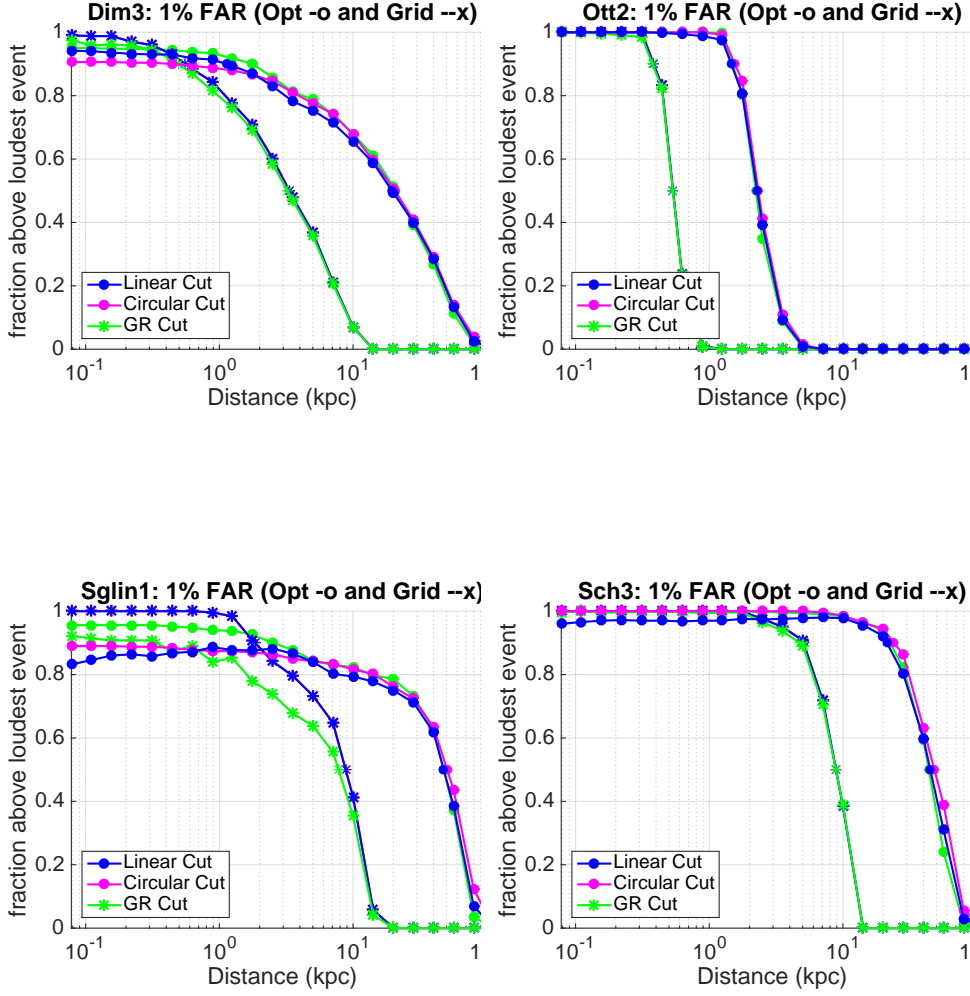


Figure 3.5: The different coherent consistency cuts use different assumptions of polarization content. The GR cuts assume a plus and cross polarized signal, the circular cut assumes a circularly polarized signal, and the linear cut assume plus polarized signal only with an arbitrary polarizations angle. The  $-x$  refers to detection efficiency for the linear grid search which consists of a grid that is sufficiently dense over the sky without being too large to process quickly. The  $-o$  refers to the detection efficiency for an optically triggered, single sky point, search. Top-Left: A linearly polarized Dimmelmeier waveform [9]. Top-Right: A 3D Ott neutrino driven convection waveform [7]. Bottom-Left: A linearly polarized sine-Gaussian waveform. Bottom-Right: A 3D rotating core-collapse waveform from Scheidegger [10].

detectors can be used to reduce the size of the grid. By overlap, I mean throwing out any sky location from the original sky grid for which the declination angle is outside of the declination angle of the Milky Way. Figure 3.8 demonstrates the results from this analysis. Depending on the GPS time, this information can reduce



the grid to as little as 60 percent of its original size. Unfortunately, the number of grid points is only reduced in 70 percent of cases. I did this analysis for every 10 minutes block of time over the course of a year starting at an arbitrarily selected date. These parameters were chosen in order to see what sort of structure the effect of using the Milky Way had on the linear grid over the course of the year. Figure 3.8 shows two days of this year and is representative of the entire year. The GPS time selected for this search coincided with a time where there was a reduction in the size of the grid. Therefore, in order to highlight the potential gain in sensitivity from this information, I constructed background and efficiency curves for this new linear grid. Although this did reduce the significance of the background and improve the location of the GWBs on the coherent and incoherent energy plane, there were still no cuts selected and the efficiency curves only improved slightly. Figure 3.6 demonstrates the difference in background significance between the reduced linear grid and original linear grid search. The statistic selected by the post-processing was the powerlaw statistic which takes the power in each pixels and raises it to some power  $d$ . In Figure 3.7, the difference in location on the E-I plane for the plus and cross coherent statistics is shown for the two searches. The reduced grid shows an improvement in the location with the GWBs falling farther off of the line than in the linear grid case. Again, this leads me to believe that as currently implemented the analysis is failing to appropriately account for antenna response functions and thus the coherent analysis is still failing, although less than the search with the full grid. Further work will need to be completed to refine the linear grid search, but it appears with a little tweaking it will prove an effective search. Two potential options include using a linear grid constructed from the actual position of the galactic disk on the sky and using a full 2D grid with large spacing in between which can account for the antenna response more accurately.

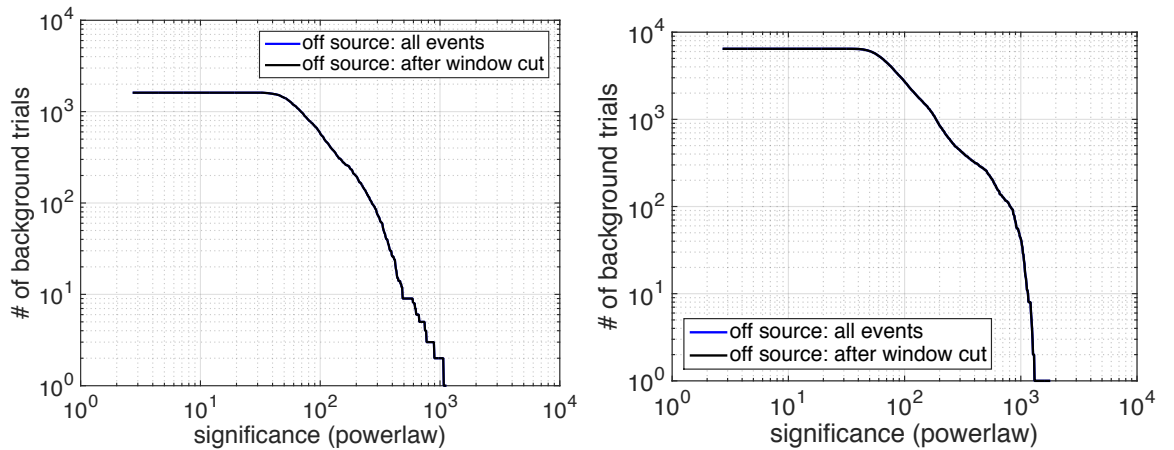


Figure 3.6: Left: The distribution of the significance (detection statistic), or “loudness”, of the background for the optical search using the powerlaw statistic. The black line represents the entire background before any coherent consistency cuts are made and in both the linear grid and reduced linear grid no cuts were selected. Right: Same as the left except for the reduced linear grid search. Overall, the loudest background event is less significant in the reduced grid but by not a large margin.

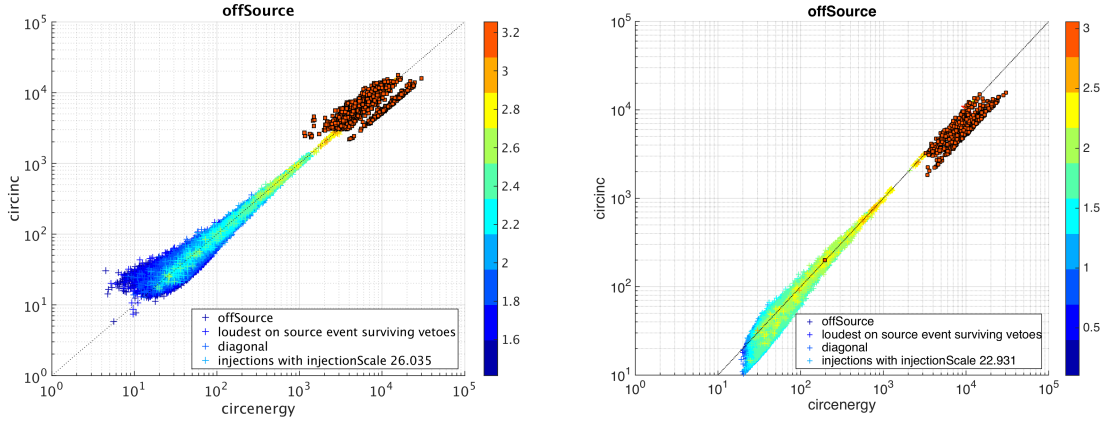


Figure 3.7: Left: Coherent versus Incoherent linear energy of the Ott 3D waveforms [7] in the linear grid search for the injection amplitude for which 90 percent of the injections were detected. Again, the signals do not appear to have any consistent pattern. Right: Same as the left except for the reduced grid search. This time a more clear pattern is emerging as these signals are starting to clearly fall to the right of the E-I line. This improvement in the reduced grid suggests that, although the time delays are appropriately accounted for, the antenna response function may be miscalculated and the coherent combination of the data is incorrect for the linear grid search.

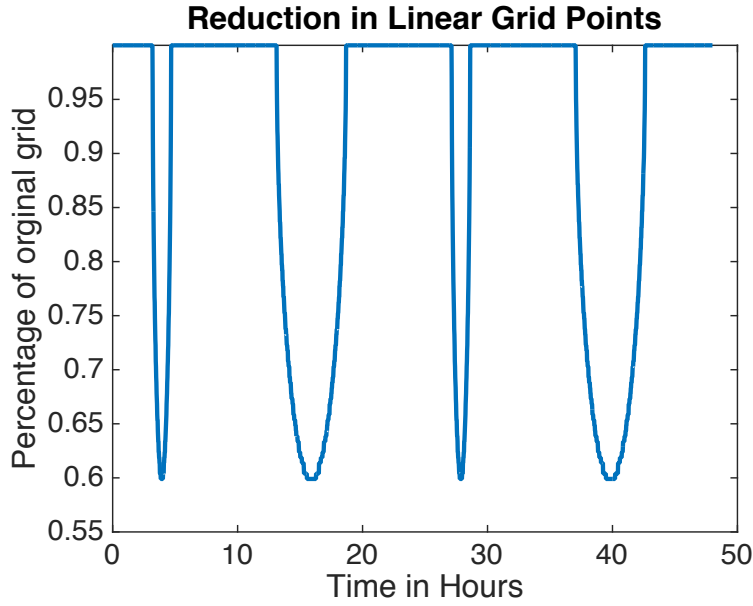


Figure 3.8: This figure shows the potential reduction in number of grid points of the linear grid search when utilizing information from the location of the MilkyWay on the sky. This information is over an arbitrarily chosen 48 hour period. The x-axis shows the percentage of the original number of grid points needed when the information from the MilkyWay is included.

### 3.5 Conclusions

In this Chapter, I explored the performance of a fast analysis for a SNEWS triggered all-sky search compared to the sensitivity of an optically-triggered analysis. Specif-

Waveform Type	Model Name	Opt. 50 % distance Circular	Opt. 50 % distance Plus/Cross	Opt. 50 % distance Linear
Rotating Core Collapse	Dim-s15A2O05ls	27.58	26.20	27.58
Rotating Core Collapse	Dim-s15A2O09ls	25.73	25.24	23.61
Rotating Core Collapse	Dim-s15A3O15ls	20.56	20.81	19.56
Rotating Core Collapse	Sch-R1E1CA-L	0.69	0.66	0.66
Rotating Core Collapse	Sch-R3E1AC-L	41.88	40.00	40.45
Rotating Core Collapse	Sch-R4E1FC-L	48.32	43.85	45.00
3D Convection	Müller-L15-3	2.12	2.05	2.08
3D Convection	Müller-N20-2	0.94	0.89	0.94
3D Convection	Müller-W15-4	1.27	1.25	1.24
3D Convection	Ott-s27	2.33	2.28	2.22

Table 3.2: We present the 50 percent detection distance at a false alarm probability of 0.1 percent utilizing the various coherent statistic and assumptions on polarization content. Across all waveforms, these coherent statistics provide nearly identical recovery distances. Nonetheless, the circular coherent consistency cuts proved best in 9 of the 10 waveforms.

ically, I tested a linear sky-grid that had been previous employed in GRB searches. In the end, the sensitivity was poor and not to astrophysical relevant distances. Further exploration indicated the problem was most likely due to antenna responses changing too much between the actual CCSN location and the linear grid points that were searched. Two solutions to this issue include using a linear grid constructed from the actual position of the galactic disk on the sky and using a larger number of grid points to cover the antenna response more accurately.

## Chapter 4

# Conclusions

This thesis has explored both the scientific benefits of gravitational wave bursts from a galactic core-collapse supernovae as well as techniques to detect these signals in detector data.

In Chapter 2, I motivated an analysis for alternative polarized signals that could arise from a galactic supernova. LIGO and Virgo are sensitive to gravitational wave signals not only from the plus and cross polarizations predicted by general relativity, but potentially also to gravitational waves predicted by alternative theories of gravity. The type of polarization I studied in my thesis is known as the scalar mode which is predicted to arise from spherically symmetric systems (unlike in general relativity, where spherically symmetric systems do not produce gravitational waves). One particular system of interest for such signals is core-collapse supernovae. Because these are nearly spherically symmetric systems, it is possible that the dominant form of emission could come in the form of scalar polarized signals. Therefore, I explored the formulation of statistics designed for the extraction of these signals from the detector data. These statistics came in the form of ranking or detection statistics and coherent statistics, which are designed to reject background noise events. After this formulation, I ran a search on a variety of possible scalar signals. These signals included waveforms from simulations of a core-collapse supernovae to neutron-star remnant, neutron-star collapse to black-hole, galactic dust collapsing to a black hole, and the spontaneous scalarization of neutron stars. I estimated the sensitivity to and feasibility of detecting these types of waveforms. I showed that scalar gravitational-waves are detectable to a few kiloparsecs with advanced LIGO, even when restricting scalar parameters to their currently constrained values. Initial runs proved promising, and it appears possible to make meaningful scientific claims about scalar-tensor theories, signals models, and the equation-of-state.

In Chapter 3, I discussed the current implementation of the low-latency SNEWS triggered X-Pipeline search. Galactic supernovae are one of the most important targets for the advanced LIGO and Virgo detectors. While the rate of a galactic supernovae is quite uncertain, they occur at most about once every 30 years. For this reason, a prompt gravitational-wave search from such an event will be important to maximize the science from these events by the astronomical community at large. Using events identified by a consortium of neutrino detectors, LIGO and Virgo will be able to perform rapid coincident searches in their detector data. The sky location information provided by such triggers is relatively poor, but the timing information is very valuable due to the limiting amount of time required for a search. I explored the ramifications of this fact by performing a simulation where a supernova trigger

has occurred but with poor sky location information. I show the loss in sensitivity between using an all-sky analysis (where the sky location is not known at all) to an optically triggered analysis (where the sky location is known). I showed a simple linear grid of time-delays is not effective for such a search due to the change in antenna response across time delays. I briefly discussed potential solutions to this issue. One potential solution is to perform a coarse two-dimensional grid search to account for the antenna factors. Another solution to speed-up the analysis is to reduce the portions of the sky searched to overlap with the Milky Way Galaxy, which can reduce the number of points by a factor of two at certain times. I also detailed the numerical supernovae waveforms used in the analysis that could arise from a variety of explosion mechanisms.

In this thesis, I have discussed improvements to existing searches using optimized sky location grids and statistics. But another potential area of improvement is in the clustering techniques. Most searches for unmodeled transients use seed-based nearest neighbor clustering of strain power spectrograms [67, 68], which identify GW signals by searching for pixels of excess power above some threshold, *seeds*, which leads to the creation of seeds along a spectrogram track. The algorithm then uses a rule to connect neighboring seeds to form a cluster. Detection statistics are then computed based on these clusters, which determine whether it is consistent with signal or noise. These algorithms are beneficial for signal morphologies that have no or few defining characteristics. For sources, such as core-collapse supernovae [69] for which numerical relativity simulations and waveform catalogs exist, a potential alternative is to use Principal Component Analysis (PCA) based catalogs to perform the clustering. “Seedless clustering,” integrates the signal power along spectrogram tracks using pre-defined “templates” chosen to capture the salient features of a wide class of signal models. We can combine the power of PCA catalogs and seedless clustering to search for gravitational-wave signals.

Original work for this project was funded by the NSF through the University of Florida’s IREU program. Final work for this project was funded by the Fulbright Scholarship through the United States Department of State.

## Chapter 5

# Appendix

### 5.1 Appendix A: Likelihood Marginalization

$$L(\mathbf{d}|h_b, \sigma_h) = \int_A L(\mathbf{d}|Ah_b)p(A)dA. \quad (5.1)$$

$L(\mathbf{d}|Ah_b)$  has the form of Eq. 2.21, where  $h_b$  is now  $Ah_b$ .

$$\int_A \exp\left((\mathbf{d} \cdot Ah_b) - \frac{1}{2}\|Ah_b\|^2\right) \frac{\exp\left(-\frac{1}{2}\frac{A^2}{\sigma_h^2}\right)}{\sqrt{2\pi\sigma_h^2}} dA \quad (5.2)$$

Next I rearrange the equation.

$$\frac{1}{\sqrt{2\pi\sigma_h^2}} \int_A \exp\left(A(\mathbf{d} \cdot h_b) - \frac{1}{2}A^2\left(\|h_b\|^2 + \frac{1}{\sigma_h^2}\right)\right) dA \quad (5.3)$$

Now, I make a couple coefficient substitutions,  $\mathbf{d} \cdot h_b = b$  and  $R = \|h_b\|^2 + \frac{1}{\sigma_h^2}$ .

$$\frac{1}{\sqrt{2\pi\sigma_h^2}} \int_A \exp\left(-\frac{1}{2}ARA + bA + 0\right) dA \quad (5.4)$$

The payoff of these substitutions and rearrangement, is that our integral now has the form of a Gauss Integral which looks like

$$\int_{R^M} \exp\left(-\frac{1}{2}\mathbf{x}^\dagger \mathbf{R} \mathbf{x} + \mathbf{b}^\dagger \mathbf{x} + c\right) d\mathbf{x} \quad (5.5)$$

The Gauss Integral has the solution

$$\sqrt{\det 2\pi \mathbf{R}^{-1}} \exp\left(\frac{1}{2}\mathbf{b}^\dagger \mathbf{R}^{-1} \mathbf{b} + c\right) \quad (5.6)$$

Therefore, in our case, the solution is

$$L(\mathbf{d}|h_b, \sigma_h) = \frac{1}{\sqrt{2\pi\sigma_h^2}} \sqrt{\det 2\pi \frac{1}{R}} \exp\left(\frac{1}{2}b\frac{1}{R}\right) \quad (5.7)$$

$$L(\mathbf{d}|h_b, \sigma_h) = \frac{\sqrt{\frac{1}{R}}}{\sqrt{\sigma_h^2}} \exp\left(\frac{1}{2}b\frac{1}{R}\right) \quad (5.8)$$

Finally, I take the log of both sides and plug back in for R and b.

$$\log(L(\mathbf{d}|h_b, \sigma_h)) = \left(\frac{1}{2}b\frac{1}{R}\right) + \log\left(\frac{1}{\sqrt{R\sigma_h^2}}\right) \quad (5.9)$$

$$\left(\frac{1}{2}\mathbf{d} \cdot h_b \frac{1}{||h_b||^2 + \frac{1}{\sigma_h^2}}\right) + \log\left(\frac{1}{\sqrt{\left(||h_b||^2 + \frac{1}{\sigma_h^2}\right)\sigma_h^2}}\right) \quad (5.10)$$

$$\frac{1}{2}\left(\frac{\mathbf{d} \cdot h_b}{||h_b||^2 + \frac{1}{\sigma_h^2}}\right) + \log\left(\frac{1}{\sqrt{\sigma_h^2||h_b||^2 + 1}}\right) \quad (5.11)$$

$$\frac{1}{2}\left(\frac{\mathbf{d} \cdot h_b}{||h_b||^2 + \frac{1}{\sigma_h^2}}\right) + \log\left((\sigma_h^2||h_b||^2 + 1)^{-\frac{1}{2}}\right) \quad (5.12)$$

$$\frac{1}{2}\left(\frac{\mathbf{d} \cdot h_b}{\left(||h_b||^2 + \frac{1}{\sigma_h^2}\right)} - \log(\sigma_h^2||h_b||^2 + 1)\right) \quad (5.13)$$

## 5.2 Appendix B: Detection Statistic Substitution

The two substitutions that need to be made are  $\mathbf{e}^b||h_b|| = h_b$  and  $||h_b|| = \frac{h_b}{\mathbf{e}^b}$ . Also, for our analysis  $||h_b|| = ||f_b||$ .

$$L(\mathbf{d}|h_b, \sigma_h) = \frac{(\mathbf{d} \cdot h_b)^2}{||h_b||^2 + \frac{1}{\sigma_h^2}} - \log(\sigma_h||h_b||^2 + 1) \quad (5.14)$$

$$L(\mathbf{d}|h_b, \sigma_h) = \frac{(\mathbf{d} \cdot \mathbf{e}^b||h_b||)^2}{||h_b||^2 + \frac{1}{\sigma_h^2}} - \log(\sigma_h||h_b||^2 + 1) \quad (5.15)$$

$$L(\mathbf{d}|h_b, \sigma_h) = \frac{\frac{1}{||h_b||^2} ||h_b||^2 (\mathbf{d} \cdot \mathbf{e}^b)^2}{\frac{1}{||h_b||^2} ||h_b||^2 + \frac{1}{\sigma_h^2}} - \log(\sigma_h||h_b||^2 + 1) \quad (5.16)$$

$$L(\mathbf{d}|h_b, \sigma_h) = \frac{(\mathbf{d} \cdot \mathbf{e}^b)^2}{1 + \frac{1}{(\sigma_h||f_b||)^2}} - \log(\sigma_h||f_b||^2 + 1) \quad (5.17)$$

$$\max_{h_b} \left( \frac{(h_b^* \cdot h_b)^2}{||h_b||^2} \right) = \max_{\mathbf{e}^b} \frac{(h_b^* \cdot ||h_b||\mathbf{e}^b)^2}{||h_b||^2} \quad (5.18)$$

$$\max_{\mathbf{e}^b} \frac{(h_b^* \cdot ||h_b||\mathbf{e}^b)^2}{||h_b||^2} = \max_{\mathbf{e}^b} (h_b^* \cdot \mathbf{e}^b)^2 \quad (5.19)$$

# Bibliography

- [1] Gregory M. Harry. Advanced LIGO: The next generation of gravitational wave detectors. *Class.Quant.Grav.*, 27:084006, 2010. doi: 10.1088/0264-9381/27/8/084006.
- [2] Masaru Shibata, Kenichi Nakao, and Takashi Nakamura. Scalar-type gravitational wave emission from gravitational collapse in brans-dicke theory: Detectability by a laser interferometer. *Phys. Rev. D*, 50:7304–7317, Dec 1994. doi: 10.1103/PhysRevD.50.7304. URL <http://link.aps.org/doi/10.1103/PhysRevD.50.7304>.
- [3] Jerome Novak and Jose Ibanez. Gravitational waves from the collapse and bounce of a stellar core in tensor-scalar gravity. *Astrophys. J.*, 533(1):392, 2000. URL <http://stacks.iop.org/0004-637X/533/i=1/a=392>.
- [4] Jérôme Novak. Spherical neutron star collapse toward a black hole in a tensor-scalar theory of gravity. *Phys. Rev. D*, 57:4789–4801, Apr 1998. doi: 10.1103/PhysRevD.57.4789. URL <http://link.aps.org/doi/10.1103/PhysRevD.57.4789>.
- [5] B. Bertotti, L. Iess, and P. Tortora. A test of general relativity using radio links with the cassini spacecraft. *Nature*, 425(6956):374–376, 09 2003. URL <http://dx.doi.org/10.1038/nature01997>.
- [6] Paulo C. C. Freire, Norbert Wex, Gilles Esposito-Farèse, Joris P. W. Verbiest, Matthew Bailes, Bryan A. Jacoby, Michael Kramer, Ingrid H. Stairs, John Antoniadis, and Gemma H. Janssen. The relativistic pulsar-white dwarf binary psr j1738+0333 ? ii. the most stringent test of scalar-tensor gravity. *Monthly Notices of the Royal Astronomical Society*, 423(4):3328–3343, 2012.
- [7] C. D. Ott, E. Abdikamalov, P. Mösta, R. Haas, S. Drasco, E. P. O’Connor, C. Reisswig, C. A. Meakin, and E. Schnetter. General-relativistic Simulations of Three-dimensional Core-collapse Supernovae. , 768:115, May 2013.
- [8] B. Müller, H.-T. Janka, and A. Marek. A New Multi-dimensional General Relativistic Neutrino Hydrodynamics Code of Core-collapse Supernovae. III. Gravitational Wave Signals from Supernova Explosion Models. , 766:43, 2013. doi: 10.1088/0004-637X/766/1/43.
- [9] H. Dimmelmeier, C. D. Ott, A. Marek, and H.-T. Janka. Gravitational wave burst signal from core collapse of rotating stars. , 78:064056, 2008.
- [10] S. Scheidegger, S. C. Whitehouse, R. Käppeli, and M. Liebendörfer. Gravitational waves from supernova matter. , 27:114101, June 2010.



- 
- [11] Michal Was, Patrick J. Sutton, Gareth Jones, and Isabel Leonor. Performance of an externally triggered gravitational-wave burst search. *Phys.Rev.*, D86:022003, 2012. doi: 10.1103/PhysRevD.86.022003.
  - [12] S. E. Gossan et al. Observing Gravitational Waves from Core-Collapse Supernovae. *In preparation, LIGO-P1400233*, 2015.
  - [13] Hans Ohanian and Remo Ruffini. *Gravitation and Spacetime*. W.W. Norton and Company, 2nd edition, 1976.
  - [14] C. Brans and R. H. Dicke. Mach’s principle and a relativistic theory of gravitation. *Phys. Rev.*, 124:925–935, Nov 1961. doi: 10.1103/PhysRev.124.925. URL <http://link.aps.org/doi/10.1103/PhysRev.124.925>.
  - [15] Nicols Yunes and Xavier Siemens. Gravitational-Wave Tests of General Relativity with Ground-Based Detectors and Pulsar Timing-Arrays. *Living Rev.Rel.*, 16:9, 2013. doi: 10.12942/lrr-2013-9.
  - [16] J.M. Weisberg and J.H. Taylor. Relativistic binary pulsar b1913+16: Thirty years of observations and analysis. *Binary Radio Pulsars, Proc. Aspen Conference, ASP Conf. Series*, 2004.
  - [17] J. Weber. Detection and generation of gravitational waves. *Phys. Rev.*, 117(1):306–313, Jan 1960. doi: 10.1103/PhysRev.117.306.
  - [18] Francesco Ronga. Detection of gravitational waves with resonant antennas. *Journal of Physics: Conference Series*, 39(1):18, 2006. URL <http://stacks.iop.org/1742-6596/39/i=1/a=005>.
  - [19] Rana Adhikari. *Sensitivity and noise analysis of 4 km laser interferometric gravitational wave antennae*. PhD thesis, Massachusetts Institute of Technology, 2004.
  - [20] Abbott B. et al. LIGO: The Laser Interferometer Gravitational-Wave Observatory. *Reports on Progress in Physics*, 72:076901, 2009.
  - [21] Acernese F. et al. Status of Virgo. *Classical and Quantum Gravity*, 25:114045, 2008. doi: <http://iopscience.iop.org/0264-9381/25/11/114045>.
  - [22] Grote H. for the LIGO Scientific Collaboration. The GEO 600 status. *Class. Quantum Grav.*, 27:084003, 2010.
  - [23] M Punturo et al. The einstein telescope: a third-generation gravitational wave observatory. *Classical and Quantum Gravity*, 27(19), 2010. URL <http://iopscience.iop.org/0264-9381/27/19/194002/>.
  - [24] Karsten Danzmann and the LISA study team. Lisa: laser interferometer space antenna for gravitational wave measurements. *Classical and Quantum Gravity*, 13(11A):A247, 1996. URL <http://stacks.iop.org/0264-9381/13/i=11A/a=033>.
  - [25] The LIGO Scientific Collaboration and The Virgo Collaboration. An upper limit on the stochastic gravitational-wave background of cosmological origin. *Nature*, 460:990, 2009.

- [26] J. Aasi et al. Targeted search for Gravitational-Waves from Core-Collapse Supernovae in initial LIGO and Virgo data. *To be submitted to Phys. Rev. D., LIGO-P1400208*, 2014. URL <https://dcc.ligo.org/LIGO-P1400208>.
- [27] P. J. Sutton, G. Jones, S. Chatterji, P. Kalmus, I. Leonor, S. Poprocki, J. Rollins, A. Searle, L. Stein, M. Tinto, and M. Was. X-Pipeline: an analysis package for autonomous gravitational-wave burst searches. *New Journal of Physics*, 12:053034–+, 2010.
- [28] S. Klimenko, S. Mohanty, M. Rakhmanov, and G. Mitselmakher. Constraint likelihood analysis for a network of gravitational wave detectors. *Phys. Rev. D*, 72:122002, Dec 2005. doi: 10.1103/PhysRevD.72.122002. URL <http://link.aps.org/doi/10.1103/PhysRevD.72.122002>.
- [29] S Klimenko, I Yakushin, A Mercer, and G Mitselmakher. Coherent method for detection of gravitational wave bursts. *Class. Quant. Grav.*, 25:114029, 2008.
- [30] Eric Thrane et al. Long gravitational-wave transients and associated detection strategies for a network of terrestrial interferometers. *Physical Review D*, 83:083004, 2011.
- [31] Warren G. Anderson, Patrick R. Brady, Jolien D. E. Creighton, and Éanna É. Flanagan. Excess power statistic for detection of burst sources of gravitational radiation. *Phys. Rev. D*, 63:042003, Jan 2001. doi: 10.1103/PhysRevD.63.042003. URL <http://link.aps.org/doi/10.1103/PhysRevD.63.042003>.
- [32] Michal Was. Searching for gravitational waves associated with gamma-ray bursts in 2009-2010 LIGO-Virgo data. 2011.
- [33] Paul D. Scharre and Clifford M. Will. Testing scalar-tensor gravity using space gravitational-wave interferometers. *Phys. Rev. D*, 65:042002, Jan 2002. doi: 10.1103/PhysRevD.65.042002. URL <http://link.aps.org/doi/10.1103/PhysRevD.65.042002>.
- [34] Kent Yagi and Takahiro Tanaka. Constraining alternative theories of gravity by gravitational waves from precessing eccentric compact binaries with lisa. *Phys. Rev. D*, 81:064008, Mar 2010. doi: 10.1103/PhysRevD.81.064008. URL <http://link.aps.org/doi/10.1103/PhysRevD.81.064008>.
- [35] F. Acernese et al. Advanced Virgo Preliminary Design. *Virgo Internal report: VIR-0089A-08*, 2008.
- [36] Kentaro Somiya. Detector configuration of KAGRA: The Japanese cryogenic gravitational-wave detector. *Class.Quant.Grav.*, 29:124007, 2012. doi: 10.1088/0264-9381/29/12/124007.
- [37] C. D. Ott. TOPICAL REVIEW: The gravitational-wave signature of core-collapse supernovae. *Class. Quantum Grav.*, 26:063001, 2009. doi: 10.1088/0264-9381/26/6/063001.
- [38] K. Kotake. Multiple physical elements to determine the gravitational-wave signatures of core-collapse supernovae. *Comptes Rendus Physique*, 14:318, 2013. doi: 10.1016/j.crhy.2013.01.008.

- 
- [39] Peter Shawhan. Detectability of scalar gravitational-wave bursts with ligo and virgo. *ArXiv*, 2014. doi: 10.1007/s10714-014-1720-4.
  - [40] Cadonati et al. The LSC-Virgo White Paper on Gravitational Wave Searches and Astrophysics. <https://dcc.ligo.org/LIGO-T1400054/public>, pages 143–148, 2015.
  - [41] M. Ikeda et al. Search for Supernova Neutrino Bursts at Super-Kamiokande. , 669:519, nov 2007. doi: 10.1086/521547.
  - [42] E. Abdikamalov, S. Gossan, A. M. DeMaio, and C. D. Ott. Measuring the angular momentum distribution in core-collapse supernova progenitors with gravitational waves. , 90(4):044001, 2014. doi: 10.1103/PhysRevD.90.044001.
  - [43] W. J. Engels, R. Frey, and C. D. Ott. Multivariate regression analysis of gravitational waves from rotating core collapse. , 90(12):124026, December 2014. doi: 10.1103/PhysRevD.90.124026.
  - [44] C. D. Ott. Probing the core-collapse supernova mechanism with gravitational waves. *Class. Quant. Grav.*, 26(20):204015, October 2009. doi: 10.1088/0264-9381/26/20/204015.
  - [45] J. Logue, C. D. Ott, I. S. Heng, P. Kalmus, and J. Scargill. Inferring Core-Collapse Supernova Physics with Gravitational Waves. , 86(4):044023, 2012. doi: 10.1103/PhysRevD.86.044023.
  - [46] J. W. Murphy, C. D. Ott, and A. Burrows. A Model for Gravitational Wave Emission from Neutrino-Driven Core-Collapse Supernovae. , 707:1173, 2009.
  - [47] K. N. Yakunin, P. Marronetti, A. Mezzacappa, S. W. Bruenn, C.-T. Lee, M. A. Chertkow, W. R. Hix, J. M. Blondin, E. J. Lentz, O. E. Bronson Messer, and S. Yoshida. Gravitational waves from core collapse supernovae. *Class. Quantum Grav.*, 27:194005, October 2010.
  - [48] T. Fischer, S. C. Whitehouse, A. Mezzacappa, F.-K. Thielemann, and M. Liebendorfer. The neutrino signal from protoneutron star accretion and black hole formation. , 499:1–15, 2009. doi: 10.1051/0004-6361/200811055.
  - [49] C. D. Ott, C. Reisswig, E. Schnetter, E. O’Connor, U. Sperhake, F. Löffler, P. Diener, E. Abdikamalov, I. Hawke, and A. Burrows. Dynamics and Gravitational Wave Signature of Collapsar Formation. *Phys. Rev. Lett.*, 106:161103, 2011.
  - [50] C.L. Fryer, D.E. Holz, and S.A. Hughes. Gravitational Wave Emission from Core Collapse of Massive Stars. , 565:430, 2002.
  - [51] A. L. Piro and E. Pfahl. Fragmentation of Collapsar Disks and the Production of Gravitational Waves. , 658:1173, April 2007.
  - [52] Tomohiro Harada, Takeshi Chiba, Ken-ichi Nakao, and Takashi Nakamura. Scalar gravitational wave from oppenheimer-snyder collapse in scalar-tensor theories of gravity. *Phys. Rev. D*, 55:2024–2037, Feb 1997. doi: 10.1103/PhysRevD.55.2024. URL <http://link.aps.org/doi/10.1103/PhysRevD.55.2024>.
-

- [53] B.S. Sathyaprakash and Bernard F. Schutz. Physics, astrophysics and cosmology with gravitational waves. *Living Reviews in Relativity*, 12(2), 2009. doi: 10.12942/lrr-2009-2. URL <http://www.livingreviews.org/lrr-2009-2>.
- [54] J Abadie, BP Abbott, R Abbott, TD Abbott, M Abernathy, T Accadia, F Acernese, C Adams, R Adhikari, C Affeldt, et al. Search for gravitational waves from low mass compact binary coalescence in ligos sixth science run and virgos science runs 2 and 3. *Physical Review D*, 85(8):082002, 2012.
- [55] Antony C Searle, Patrick J Sutton, Massimo Tinto, and Graham Woan. Robust bayesian detection of unmodelled bursts. *Classical and Quantum Gravity*, 25(11):114038, 2008. URL <http://stacks.iop.org/0264-9381/25/i=11/a=114038>.
- [56] Jérôme Novak. Neutron star transition to a strong-scalar-field state in tensor-scalar gravity. *Phys. Rev. D*, 58:064019, Aug 1998. doi: 10.1103/PhysRevD.58.064019. URL <http://link.aps.org/doi/10.1103/PhysRevD.58.064019>.
- [57] Pietro Antonioli, Richard Tresch Fienberg, Fabrice Fleurot, Yoshiyuki Fukuda, Walter Fulgione, et al. SNEWS: The Supernova Early Warning System. *New J.Phys.*, 6:114, 2004. doi: 10.1088/1367-2630/6/1/114.
- [58] C. Vigorito and LVD Collaboration. Galactic supernovae monitoring at LVD. *Nuclear Physics B Proceedings Supplements*, 221:410–410, December 2011. doi: 10.1016/j.nuclphysbps.2011.10.054.
- [59] T. Gaisser and F. Halzen. Icecube. *Ann. Rev. Nuc. Part. Sc.*, 64(1):101, 2014.
- [60] G Alimonti, C Arpesella, H Back, M Balata, D Bartolomei, A De Bellefon, G Bellini, J Benziger, A Bevilacqua, D Bondi, et al. The borexino detector at the laboratori nazionali del gran sasso. *Nuclear Instruments and Methods in Physics Research Section A: Accelerators, Spectrometers, Detectors and Associated Equipment*, 600(3):568–593, 2009.
- [61] Daya Bay Collaboration. A side-by-side comparison of daya bay antineutrino detectors. *Nuclear Instruments and Methods in Physics Research Section A: Accelerators, Spectrometers, Detectors and Associated Equipment*, 685: 78 – 97, 2012. ISSN 0168-9002. doi: <http://dx.doi.org/10.1016/j.nima.2012.05.030>. URL <http://www.sciencedirect.com/science/article/pii/S016890021200530X>.
- [62] KamLAND Collaboration. First results from kamland: Evidence for reactor antineutrino disappearance. *Phys. Rev. Lett.*, 90:021802, Jan 2003. doi: 10.1103/PhysRevLett.90.021802. URL <http://link.aps.org/doi/10.1103/PhysRevLett.90.021802>.
- [63] SNO Collaboration. The sudbury neutrino observatory. *Nuclear Instruments and Methods in Physics Research Section A: Accelerators, Spectrometers, Detectors and Associated Equipment*, 449(12):172 – 207, 2000. ISSN 0168-9002. doi: [http://dx.doi.org/10.1016/S0168-9002\(99\)01469-2](http://dx.doi.org/10.1016/S0168-9002(99)01469-2). URL <http://www.sciencedirect.com/science/article/pii/S0168900299014692>.
- [64] J. F. Beacom and P. Vogel. Can a supernova be located by its neutrinos? , 60 (3):033007, 1999. doi: 10.1103/PhysRevD.60.033007.

- 
- [65] G. Pagliaroli, F. Vissani, E. Coccia, and W. Fulgione. Neutrinos from Supernovae as a Trigger for Gravitational Wave Search. *Phys. Rev. Lett.*, 103(3):031102, July 2009.
- [66] J. et al. Aasi. Methods and results of a search for gravitational waves associated with gamma-ray bursts using the geo 600, ligo, and virgo detectors. *Phys. Rev. D*, 89:122004, Jun 2014. doi: 10.1103/PhysRevD.89.122004. URL <http://link.aps.org/doi/10.1103/PhysRevD.89.122004>.
- [67] E Thrane and M Coughlin. Searching for gravitational-wave transients with a qualitative signal model: seedless clustering strategies. 88:083010, 2013.
- [68] T. Prestegard and E. Thrane. Burstegard: a hierarchical clustering algorithm. *LIGO DCC*, page L1200204, 2012. <https://dcc.ligo.org/cgi-bin/DocDB/ShowDocument?docid=93146>.
- [69] Christian D Ott. The gravitational-wave signature of core-collapse supernovae. *Classical and Quantum Gravity*, 26(6):063001, 2009. URL <http://stacks.iop.org/0264-9381/26/i=6/a=063001>.